Geosci. Model Dev., 18, 8535–8568, 2025
https://doi.org/10.5194/gmd-18-8535-2025

Geoscientific Model Development
Open Access
EGU

Evaluating the E3SMv2-MPAS ocean–sea ice coupled unstructured model in the Arctic: Atlantification processes and systematic biases

Xinyuan Lv[1], Huizan Wang[1], Yu Cao[1], Kaijun Ren[1], Yangjun Wang[2], and Hao Ding[1]

[1]College of Meteorology and Oceanology, National University of Defense Technology, Changsha, 410073, China
[2]College of Advanced Interdisciplinary Studies, National University of Defense Technology, Nanjing, 211101, China

Correspondence: Huizan Wang (wanghuizan@126.com) and Kaijun Ren (renkaijun@nudt.edu.cn)

Received: 5 June 2025 – Discussion started: 10 July 2025
Revised: 17 October 2025 – Accepted: 18 October 2025 – Published: 14 November 2025

Abstract. Advancing high-resolution Arctic ocean–sea ice modeling is critical for understanding polar amplification and improving climate projections but faces challenges from computational limits and cross-scale interactions. The simulation capabilities of the ocean–sea ice coupled model (E3SMv2-MPAS) from the Energy Exascale Earth System Model (E3SM) 2.1 for the Arctic ocean–sea ice system are systematically evaluated using multi-source observational data. The model employs a latitudinally varying mesh, with resolution increasing from 60 km in the Southern Hemisphere to 10 km in the Arctic. This design balances computational efficiency with the accurate integration of low-latitude oceanic influences, while the unstructured mesh also enhances the geometric representation of Arctic straits. Together, these features form a simulation framework capable of resolving processes from seasonal to decadal timescales. Numerical results demonstrate E3SMv2-MPAS's superior Arctic simulation performance: (1) accurate reproduction of spatial heterogeneity in sea ice concentration, thickness, and sea surface temperature, including their 1995–2020 trend patterns; (2) faithful reproduction of both the freshwater content and transports through key Arctic gateways; (3) successful reconstruction of three-dimensional thermohaline structures within the Atlantic Water layer, capturing Atlantic Water's decadal warming trends and accelerated Atlantification processes – specifically mid-layer shoaling, heat content amplification, and reduced heat transfer lag times in the Eurasian Basin. Persistent systematic biases are identified: 0.5–1 m sea ice thickness overestimation in the Canadian Basin; Coordinated sea surface temperature/salinity underestimation and sea ice concentration overestimation in the Greenland and Barents Seas; Atlantic Water core temperature overestimation; Regional asymmetries in decadal thermohaline field evolution.

1 Introduction

The Arctic region has emerged as one of the most rapidly transforming area of the Earth system under contemporary climate change (Calvin et al., 2023). However, persistent gaps in oceanic observational networks, particularly the lack of systematic full-depth and pan-strait measurements across key Arctic gateways, have significantly constrained our understanding of Arctic oceanic transport dynamics. To address these observational limitations, numerical modeling has become an indispensable tool (Wang et al., 2023). Of particular scientific significance is the thermohaline transport through Fram Strait – the principal conduit for Atlantic Water (AW) intrusion into the Arctic basins (Fu et al., 2023; Karami et al., 2021; Long et al., 2024). Recent studies highlight the necessity to quantify both the spatiotemporal evolution of AW-derived heat distribution across Arctic marginal seas and the relative contributions of different vertical heat flux mechanisms (Carmack et al., 2015; Polyakov et al., 2020b). State-of-the-art global climate models (GCMs) provide critical insights into the evolving climate system under sustained global warming scenarios, enabling the investigation of multi-sphere interactions and their associated feedback mechanisms (Dörr et al., 2021; Hinrichs et al., 2021; Rieke et al., 2023; Shu et al., 2022).

While climate models remain indispensable tools for deciphering Earth system dynamics (Landrum and Holland, 2020), their representation of Arctic processes exhibits per-

sistent uncertainties that challenge predictive capabilities (Pan et al., 2023). Systematic biases plague the simulation of critical Arctic phenomena, including amplified warming rates, sea ice retreat patterns, and AW layer evolution (Heuzé et al., 2023; Khosravi et al., 2022; Muilwijk et al., 2023; Shu et al., 2019). These limitations persist across successive model generations, as evidenced by Coupled Model Intercomparison Project Phase 5 (CMIP5) and Phase 6 (CMIP6) revealing substantial errors in Arctic three-dimensional thermohaline structure reproduction (Khosravi et al., 2022; Shu et al., 2019). There are mainly four common biases of contemporary models in the Arctic include: (1) overestimated AW layer thickness and depth. This systematic vertical structure misrepresentation persists across model generations, from early Arctic Ocean Model Intercomparison Project (AOMIP) simulations (Holloway et al., 2007) through the Coordinated Ocean-ice Reference Experiments, phase II (CORE-II; Ilıcak et al., 2016), to the most widely used CMIP5/CMIP6 ensembles (Heuzé et al., 2023; Khosravi et al., 2022; Shu et al., 2019). Among 41 CMIP5 models evaluated by Shu et al. (2019), 22 % failed basic AW identification criteria, while the remaining 32-model mean overestimated AW layer vertical extent compared to observational benchmarks. CMIP6 shows limited improvement, with multi-model mean AW upper boundaries erroneously positioned at ~ 400 m depth in the Nansen Basin – deeper than observed values – and excessive thickness extending to the seafloor in some regions (Khosravi et al., 2022). (2) Cold bias in AW core temperatures. The Alfred Wegener Institute coupled climate model (AWI-CM1) exhibits thermal underestimation at 200–600m depths in Eurasian Basin simulations (Hinrichs et al., 2021), consistent with CMIP6's 0.4 °C cold bias relative to hydrographic climatologies (Heuzé et al., 2023). (3) Failure to capture AW warming trends. CMIP5 models collectively underestimate observed decadal temperature variability, with no model replicating the post-2000 acceleration in AW warming (Shu et al., 2019). (4) Underestimated "Atlantification" (referring to the Arctic Ocean water properties becoming increasingly akin to the warmer and saltier AW). While models project gradual boreal water encroachment in the Barents Sea by 2100 (Wassmann et al., 2015), observational analyses suggest this regime shift is likely to occur at a faster pace (Lind et al., 2018). Discrepancies extend to sea ice thermodynamics, where Seasonal Forecast System 5 (SEAS5) simulations yield only 10–20 cm winter ice production decline (Polyakov et al., 2022), versus 78–93 cm observed losses (Polyakov et al., 2020b).

There are numerous and complex reasons that lead to the common deviations in models when simulating the AW. These challenges can be categorized into four primary domains: (1) insufficient horizontal resolution (> 50 km in most CMIP6 models) fails to resolve critical boundary currents and mesoscale eddies (Hinrichs et al., 2021); (2) unrealistic Atlantic-Arctic exchange through Fram Strait (Hinrichs et al., 2021); (3) parameterization deficiencies, including the incorrect representation of horizontal advection and vertical mixing (Lind et al., 2018); (4) imperfect knowledge of ocean–sea ice–atmosphere triadic feedbacks, especially during winter convection events, hampers accurate simulation of AW ventilation processes (Heuzé et al., 2023). To advance model fidelity and reduce uncertainty sources, comprehensive investigations into systematic model biases are imperative (Hinrichs et al., 2021; Pan et al., 2023).

Current numerical simulations for polar regions are primarily based on structured grid models. However, the inherent limitations of structured grids, particularly the singularity at the North Pole and meridional convergence artifacts, fundamentally constrain their capacity to represent Arctic-specific physical processes (Liu et al., 2016). These geometric constraints not only distort parameterization schemes but also introduce systematic biases in both regional and decadal-scale simulations. While global high-resolution configurations could theoretically mitigate such issues, their prohibitive computational costs render them impractical for climate-scale applications (Golaz et al., 2019). This technological impasse has driven the development of two complementary approaches: (1) nested grid systems: Though offering advantages in spatial discretization flexibility and geometric simplification, their implementation introduces nontrivial challenges in mass conservation, interface coupling fidelity, and numerical noise suppression (Hoch et al., 2020). (2) Unstructured mesh: by enabling localized resolution enhancement in dynamically critical zones while maintaining coarse resolutions elsewhere, these meshes eliminate the need for explicit nesting procedures (Scholz et al., 2019). Their continuous spatial adaptability allows direct resolution of sub-mesoscale processes without compromising computational efficiency (Wang et al., 2018).

The application of variable-resolution models with a global unstructured mesh offers distinct advantages for Arctic Ocean studies. By employing high-resolution meshes over the Arctic region, these configurations enable accurate simulation of energy exchange processes across narrow critical channels (e.g., Fram Strait, Bering Strait, Barents Sea Opening and Davis Strait). Coarser resolutions in other domains maintain computational efficiency while preserving connectivity between the Arctic and extratropical regions (Wang et al., 2018). Among global implementations, two widely adopted models are the Finite-Volume Coastal Ocean Model (FVCOM; Chen et al., 2016) and the Finite-Element Sea ice-Ocean circulation Model (FESOM; Danilov et al., 2017). In Arctic studies, FVCOM predominantly operates as a regional model, as evidenced by its frequent implementation in localized domains (e.g., Zhang et al., 2016). This regional focus aligns with FVCOM's original design paradigm prioritizing coastal and shelf-sea dynamics through its finite-volume discretization scheme. In contrast, FESOM has been predominantly implemented as a global model in Arctic studies, where its implementation has demonstrated

unprecedented skill in simulating Arctic intermediate water dynamics (Danilov et al., 2017; Wang et al., 2018; Wekerle et al., 2013). Notably, Wang et al. (2018) established that FESOM (a relatively low resolution, ∼ 24 km in the Arctic) outperforms a set of the state-of-the-art structured-grid models evaluated by Ilıcak et al. (2016), particularly in correcting systematic AW core biases.

As a more recent modeling framework relative to FESOM and FVCOM, the Model for Prediction Across Scales (MPAS) remains in the nascent phase of Arctic performance evaluation (Huo et al., 2025; Ringler et al., 2013), particularly regarding its capacity to simulate intermediate water masses and Atlantification processes. The Energy Exascale Earth System Model (E3SM), evolved from the Community Earth System Model (CESM), incorporates MPAS-Ocean and MPAS-Seaice as its ocean and sea ice components. Initial assessments using E3SMv1's ocean–sea ice coupled configuration (60 to 10 km variable resolution) demonstrate promising skill in reproducing pan-Arctic freshwater budgets, gateway current exchanges, and vertical hydrographic profiles (Veneziani et al., 2022). Persistent errors in sea ice thickness (SIT) distribution and upper 100 m stratification emerge across resolutions, suggesting common structural model deficiencies rather than discretization artifacts. However, their diagnostic lack the rigorous validation metrics employed by Wang et al. (2018) for FESOM's AW representation. Existing assessments predominantly rely on pan-Arctic-basin-averaged diagnostics, obscuring critical vertical and regional heterogeneities in intermediate AW layer dynamics (Veneziani et al., 2022).

This study presents a tripartite evaluation framework for the coupled system of MPAS-Ocean and MPAS-Seaice in E3SM version 2 (E3SMv2-MPAS), which compares it with the observational datasets and reanalysis products to systematically assess MPAS's capacity in simulating key Arctic processes. In addition, we conduct a comprehensive assessment of Arctic sea ice dynamics, surface layer hydrographic properties, three-dimensional thermohaline profile evolution (particular emphasis on the AW layer), as well as freshwater content and key gateway transports. The assessment highlights the model's strengths, identifies its limitations, and discusses potential sources of uncertainty. Innovatively, this work implements a multi-layer connectivity analysis examining cross-layer interactions between surface (10 m) and intermediate (400 m) depths.

The subsequent sections are structured as follows: Sect. 2 provides comprehensive documentation of the E3SMv2-MPAS configuration and validation datasets. Sections 3 and 4 conduct rigorous multi-faceted analyses of Arctic-specific simulations, employing both domain-wide diagnostics and sub-regional decomposition approaches. Section 5 discusses the potential advantages of higher resolution and unstructured meshes, summarizes simulated biases and their possible sources, and identifies limitations in our model design and configuration. Finally, Sect. 6 synthesizes the key findings and outlines broader implications.

2 Model configurations and data

2.1 Model configuration

Veneziani et al. (2022) demonstrated that refining mesh resolution from 10 to 6 km triples computational costs without yielding significant improvements in simulation fidelity. Their findings suggest that resolving the local Rossby radius of deformation across most Arctic regions necessitates resolutions ≤ 3 km – a requirement currently constrained by prohibitive computational demands. The model configuration in this paper is described as follows. To address the trade-off between high-resolution requirements and computational constraints, our study employs a variable-resolution unstructured mesh featuring a meridional transition from 60 km resolution in the Southern Hemisphere to 10 km in the Arctic domain (hereafter 60 to 10 km, same as Veneziani et al. (2022); Fig. 1a). This adaptive meshing approach optimizes computational efficiency while resolving critical processes: (1) Antarctic coastal regions (80–90° S) maintain a 25 km resolution to capture fine-scale dynamics; (2) the North Atlantic sector is strategically refined, transitioning from 20 to 10 km resolution earlier than the Pacific to guarantee at least 15 km resolution in the Gulf Stream extension region (∼ 40° N; Veneziani et al., 2022); (3) the North Pacific sector maintains computational efficiency while achieving approximately 10 km resolution in its subpolar region adjacent to the Arctic Ocean (north of 50° N).

Numerical stability was achieved through a 5 min baroclinic time step for ocean dynamics. For sea ice, we employed a 15 min dynamic time step and a 30-minute thermodynamic time step (a 2 : 1 ratio). MPAS-Ocean adopts finite volume discretization of primitive governing equations within a staggered C-grid framework, incorporating hydrostatic, incompressible, and Boussinesq approximation assumptions (with a z-star vertical grid) (Golaz et al., 2019). Vertical mixing processes were parameterized using the K-profile scheme (KPP; Large et al., 1994). For mesoscale eddy representation, similarly to what was done in Veneziani et al. (2022), we implemented a spatially varying Gent–McWilliams (GM) parameterization, incorporating both bolus advection and Redi isopycnal diffusion components (Gent and Mcwilliams, 1990). The eddy diffusivity coefficient (κ) was given a latitudinal dependence: $300\,\mathrm{m^2\,s^{-1}}$ in high-resolution Arctic regions (< 20 km grid spacing) to maintain moderate mixing intensity, transitioning linearly to $1800\,\mathrm{m^2\,s^{-1}}$ in low-resolution zones (> 30 km grid spacing) to compensate for unresolved eddy fluxes (Fig. 2). MPAS-Seaice builds upon the core numerical and physical framework of the Los Alamos Sea Ice Model (CICE). The dynamics are governed by the elastic-viscous-plastic (EVP)

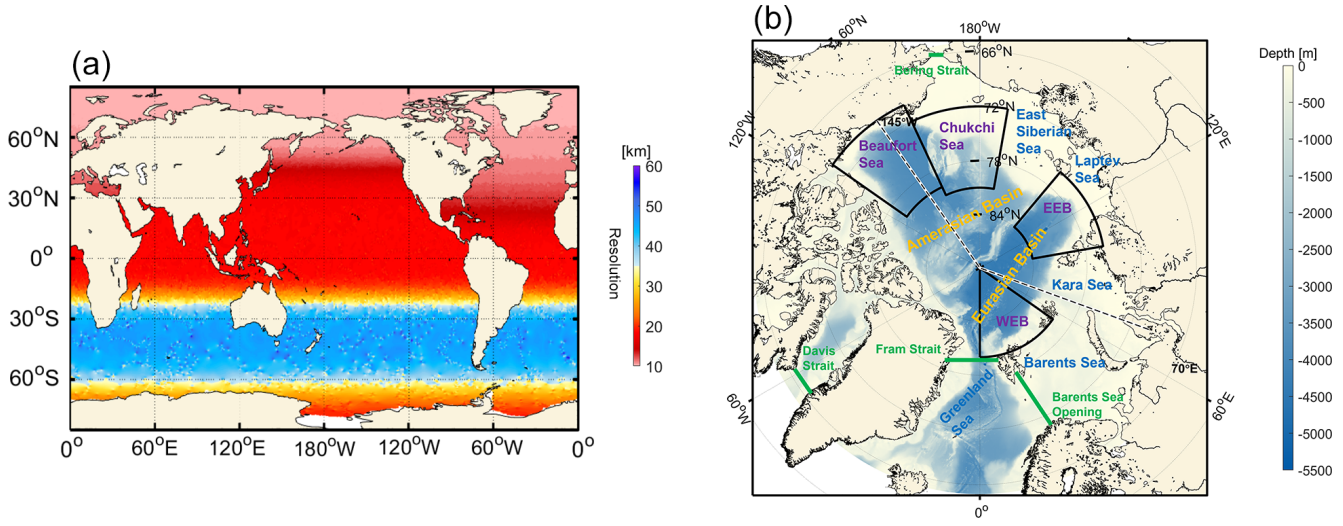

Figure 1. (a) Geographical distribution of grid cell size (km) of the E3SMv2-MPAS framework. **(b)** Bathymetry from the ETOPO 2022 and key basins/straits north of 60° N. EEB and WEB refer to the eastern and the western Eurasian Basin respectively. The black dashed transect along 70° E and 145° W (crossing the North Pole) denotes the location of the transect shown in Fig. 14.

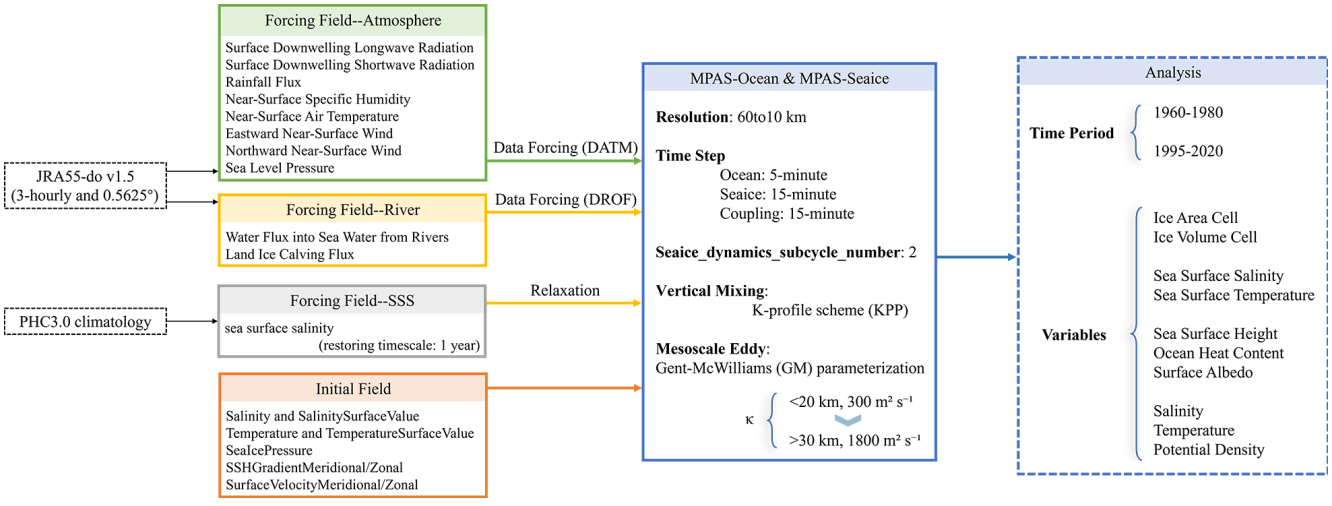

Figure 2. Configuration details for E3SMv2-MPAS: forcing/initial conditions, runtime settings, and output fields.

rheology, with the internal ice stress divergence operator adapted for MPAS's unstructured polygonal mesh (Turner et al., 2022). Sea ice and tracer transport are handled by an incremental remapping scheme (Lipscomb and Ringler, 2005), adapted for polygonal cells. The thermodynamics and vertical column physics remain consistent with CICE (Turner et al., 2022). The configuration includes the "mushy layer" thermodynamics for vertical heat transfer, the delta-Eddington shortwave radiation scheme, a level-ice melt pond parameterization, ice thickness distribution mechanics, and transport in thickness space (Petersen et al., 2019). The specific configurations of MPAS-Ocean and MPAS-Seaice within the E3SMv2, including their coupling mechanisms, have been comprehensively documented in Turner et al. (2022), Golaz et al. (2022) and Huo et al. (2025).

In addition to the ocean and sea ice components, the atmospheric and river modules in E3SMv2-MPAS (see Fig. 2 for specific variables used) were forced by the JRA55-do (v1.5; Tsujino et al., 2018) from the Japan Meteorological Agency (JMA). This dataset has high spatiotemporal resolution (3-hourly temporal and 0.5625° spatial resolution) and spans the period from 1958 to 2020. Sea surface salinity (SSS) was relaxed toward Polar science center Hydrographic Climatology (PHC) 3.0 climatology (Steele et al., 2001) with an annual restoring timescale.

Given the prohibitive computational cost of a continuous high-resolution simulation from 1958 to 2020, we adopted a

strategic two-period integration scheme to prioritize computational resources for our core analysis period (1995–2020). The model's climatological fidelity during this satellite era is verified using multi-source observational data, ensuring a reliable assessment of both sea ice and ocean variability.

The MPAS-Ocean component was initialized from a preprocessed state (ocean.ARRM60to10.180715.nc). This state was derived from a prior short-term (5 d) adjustment run of the standalone ocean model, which itself started from a state of rest with three-dimensional temperature and salinity fields prescribed from the PHC. Consequently, this initial condition provided a dynamically adjusted and physically consistent starting point for our coupled simulation, mitigating the initial shock that would otherwise occur from a purely cold start. In contrast, the MPAS-Seaice component was initialized from an idealized, uniform ice cover. A 1-meter thick ice layer with 100 % concentration was prescribed on all ocean grid points between 60° S and 70° N, with zero initial snow depth and stationary ice velocity. This simple state allowed the sea ice cover to evolve self-consistently in response to the model's atmospheric forcing and ocean coupling from the beginning of the simulation. Following this spin-up phase, the full interannual JRA55 forcing was applied from 1958 to 1981.

To begin the simulation for our main analysis period (1995–2020), we used the model state from December 1981 as the initial conditions for January 1995. This 13-year gap (1982–1994) was a strategic choice to conserve computational resources while ensuring physical consistency in the key variables of interest. This computational strategy was motivated by the fact that, under forcings such as CORE-II or JRA55 and when initialized with PHC hydrography, upper-ocean and surface variables are known to reach quasi-equilibrium within a few decades, as demonstrated in several previous studies. For instance, Wang et al. (2018) reported that temperature and salinity in the upper 1000 m reached near-equilibrium within 20–30 years. Wekerle et al. (2013) began their analysis of surface variables and freshwater content in the 0–500 m layer after a 10-year initialization in a 1958–2007 simulation using FESOM under CORE-II forcing. Likewise, in the analysis of multiple high-resolution Ocean Model Intercomparison Project Phase 2 (OMIP2) models simulating the full 1958–2020 period under JRA55 forcing, Wang et al. (2024) focused their evaluation on the period 1971–2000 – commencing approximately 13 years after the model initialization. In our simulation, the 24-year spin-up from 1958 to 1981 is largely sufficient for the adjustment of surface fields (e.g., sea ice, surface temperature, and salinity) and AW layer (above 1000 m), which are the focus of this study. Although the deep ocean remains far from equilibrium, the targeted variables had largely stabilized by 1981.

From a physical perspective, the potential impact of this initialization approach for the 1995–2020 simulation is expected to be short-lived. The upper ocean and sea ice (the primary focus of this study), adjust much more rapidly than the deep ocean, and their evolution is predominantly governed by contemporaneous atmospheric forcing rather than by the initial conditions. Therefore, the disequilibrium introduced by the initial condition from 1981 would be rapidly overwritten and adjusted by the realistic, synchronous atmospheric forcing applied from 1995 onward.

Therefore, initializing the 1995 run from the 1981 output allows a computationally efficient hot start and ensures that the model is in an appropriate state for evaluating the 1995–2020 period.

The model output initialized from the 1981 state also demonstrates physically consistent behavior during the 1995–2020 period, further supporting the validity of this approach. The temporal evolution of key diagnostic variables – including sea surface temperature (Fig. 8d) and sea ice-related variables (Fig. 7) – shows that the simulation quickly aligns with the observed/reanalysis trajectory after 1995, with no persistent systematic bias. Spatial distributions of these variables are also in good agreement with evaluation datasets (Figs. 3–5 and 8a–c), and the long-term trends from 1995 to 2020 closely match those in the references (Fig. 7). These results, which will be discussed in detail in the following sections, indicate that the initialization from 1981 did not adversely affect the simulation of central climate features during the study period.

Accordingly, our primary evaluation focuses on the performance of E3SMv2-MPAS during the period 1995–2020. In addition, a comparative assessment of the 1960–1980 period is also included to briefly examine the decadal variability of key ocean and sea ice variables and to verify the model's capability under distinctly different climatic backgrounds.

2.2 Evaluation datasets

2.2.1 Sea ice concentration, extent, thickness, and volume

To comprehensively evaluate sea ice concentration (SIC) performance, both the observations and reanalysis data were adopted for validation. SIC datasets used here include: (1) passive microwave remote sensing data: sourced from the NOAA/NSIDC Climate Data Record (Version 4; Meier et al., 2021) with a spatial resolution of 25 km × 25 km; (2) HadISST1 data: provided by the UK Met Office Hadley Centre (Rayner et al., 2003) at 1° × 1° resolution; (3) ERA5 reanalysis: Generated by the European Centre for Medium-Range Weather Forecasts (ECMWF; Hersbach et al., 2020) at 0.25° × 0.25° resolution.

For SIT validation, we utilize four key datasets: (1) Pan-Arctic Ice-Ocean Modeling and Assimilation System (PIOMAS; Zhang and Rothrock, 2003): this reanalysis product, extensively validated against satellite and in situ observations, provides reliable Arctic SIT spatial distributions and long-term trends (Laxon et al., 2013; Schweiger et al., 2011; Stroeve et al., 2014). (2) PIOMAS-20C reanalysis

(Schweiger et al., 2019): driven by ECMWF's atmospheric reanalysis of the 20th century (ERA-20C) and calibrated with historical in situ/aircraft measurements, this dataset enables analysis of pre-satellite-era SIT variability (1960–1980). (3) CS2SMOS gridded product: developed by the Alfred Wegener Institute (AWI) and the University of Hamburg (Ricker et al., 2017), it combines CryoSat-2 and SMOS satellite observations using an Optimal Interpolation method. The data cover the period from October to April each year, when the sea ice is more stable, thereby minimizing signal interference from summer melt ponds and enhancing the reliability and accuracy of the dataset.

For sea ice extent (SIE), the evaluation dataset was obtained from the NSIDC (Fetterer et al., 2017). Sea ice volume (SIV) was assessed using outputs from the PIOMAS and PIOMAS-20C reanalysis.

2.2.2 Sea surface temperature and salinity

Sea surface temperature (SST) validation dataset is NOAA's 1/4° Daily Optimum Interpolation Sea Surface Temperature (OISST; Huang et al., 2021) dataset, which represents a long-term climate data record integrating multi-platform observations from satellites, ships, buoys, and Argo floats. Spatially continuous global SST fields are reconstructed using optimal interpolation to fill data gaps.

For open-water SSS validation (SIC $< 15\,\%$), the NASA sponsored Optimum Interpolation Sea Surface Salinity (OISSS; Melnichenko et al., 2016) dataset was applied. The product integrates multi-satellite observations from Aquarius, SMAP, and SMOS through optimal interpolation. Continuous 2011–present data are generated through cross-satellite bias correction and spatial filtering, with SMOS data filling SMAP gaps.

2.2.3 Three-dimensional thermohaline

The World Ocean Atlas 2023 (WOA23; Locarnini et al., 2024; Reagan et al., 2024) served as the primary validation dataset for three-dimensional thermohaline properties. WOA23 produces high-resolution global climatological temperature and salinity fields via interpolation of historical observations (Argo floats, ship-based measurements, satellite data), covering three periods in this study: 1991–2020, 1995–2004, and 2005–2014.

To assess long-term thermohaline evolution (1960–1980 vs. 2000–2020), the UK Met Office's EN.4.2.2 dataset (Good et al., 2013) was combined. EN.4.2.2 assimilates multi-source in situ data (ship observations, Argo floats, CTD profilers, moored buoys), applies rigorous quality control, and reconstructs $1° \times 1°$ gridded temperature/salinity fields spanning 0–5500 m depth from 1900 onward.

Furthermore, annual mean temperature and salinity profiles (1970–2017) over the east Eurasian Basin, the west Eurasian Basin, the Chukchi Sea, and the Beaufort Gyre from Muilwijk et al. (2023) were included. These data derive from Russian, American, Canadian, and European expeditions, including ship/aircraft surveys, manned drifting stations, autonomous buoys, and submarine measurements.

2.2.4 Sea surface height, ocean heat content, and surface albedo

Sea surface height (SSH) evaluation data were derived from the Ocean Reanalysis System 5 (ORAS5), produced by ECMWF (Zuo et al., 2019). ORAS5 integrates multivariate observations via assimilation into the Nucleus for European Modelling of the Ocean (NEMO) ocean model coupled with the Louvain-la-Neuve sea ice model (LIM). The primary assimilated data include altimetry-based sea level anomalies from the AVISO DT2014 product, incorporating an updated mean dynamic topography. The reanalysis has a horizontal resolution of 0.25°, enhanced to approximately 9 km in the polar regions.

Ocean heat content (OHC) evaluation data were sourced from the gridded product developed by the Institute of Atmospheric Physics (IAP), Chinese Academy of Sciences (Cheng et al., 2017, 2020, 2024). It combines multi-source in situ observations – including Argo floats, CTD profiles, ship-based measurements, and moored buoys – on a $1° \times 1°$ horizontal grid. An adaptive Optimal Interpolation method is applied to minimize bias. The dataset covers the period from 1940 to present, supporting analysis of long-term oceanic changes.

Surface albedo evaluation data were obtained from the CLARA-A3 (Karlsson et al., 2023). Observations originate from multiple versions of the Advanced Very High Resolution Radiometer (AVHRR) spaceborne optical imagers employ intercalibrated radiances to mitigate intersensor discrepancies (Heidinger et al., 2010). The dataset spans from January 1979 to present, provided on a 0.25° global grid, with a 25 km equal-area grid for the polar regions.

2.2.5 Atlantic water core

Observed AW core temperature and depth data were sourced from Richards et al. (2022), comprising 55,841 profiles (1977–2018). AW core was defined as the warmest layer within salinity > 34.7 PSU profiles. To ensure accuracy, only profiles exceeding 500 m depth with sampling starting above 100 m were retained. Raw profiles were smoothed using an 80 m vertical moving average (40 m window) to remove spikes caused by thermohaline intrusions and eddies while preserving overall thermal structure.

Wang et al.'s (2024) OMIP2 dataset includes AW core temperature (defined as maximum temperature in water columns over seafloor depths > 150 m; 2006–2017) from five high-low resolution model pairs. This dataset is employed to benchmark E3SMv2-MPAS's AW core temperature simulations against multi-model ensembles.

3 Arctic physical system states

3.1 Sea ice characterization

This study focuses on the Arctic region, systematically evaluating the simulation performance of the E3SMv2-MPAS coupled model for SIC, SIT, SIE and SIV at first. Through comparisons with multi-source observational datasets and reanalysis products, combined with climate-state analysis (1995–2020) and trend diagnostics across two periods (1960–1980 and 1995–2020), model strengths and limitations in polar environmental simulations are identified.

Multi-dataset validation using NSIDC satellite remote sensing (Meier et al., 2021), Hadley in situ assimilation (Rayner et al., 2003), and ERA5 reanalysis (Hersbach et al., 2020) demonstrates that E3SMv2-MPAS effectively captures spatial heterogeneity in Arctic SIC climatology in both winter and summer (Figs. 3 and 4). In winter, consistent spatial bias patterns are observed across datasets, with persistent positive bias center ($\Delta SIC > 0.3$) identified along the southwestern Greenland Sea shelf margin and the northern Barents Sea slope (Fig. 3e–g). During summer, comparisons with NSIDC and Hadley reveal predominant positive biases in the northern Barents Sea and widespread negative biases across the central Arctic Ocean (Fig. 4e and f). In contrast, the comparison with ERA5 shows negligible underestimation in the central Arctic basin, while positive biases are observed not only in the northern Barents Sea but also in the Beaufort Sea (Fig. 4g).

Beyond SIC, SIT serves as a critical parameter governing sea ice dynamics, with its simulation accuracy directly modulating the spatiotemporal heterogeneity of ice volume. We systematically quantify E3SMv2-MPAS's capability in reproducing spatial distribution of SIT during both in winter and summer (Fig. 5). Overall, the model captures the climatological spatial gradient of Arctic SIT, characterized by a gradual thickening from the Barents Sea toward the central Arctic Basin and the northern Canadian Archipelago in both seasons. The model realistically represents the seasonal reduction in SIT over the continental shelf regions along the Arctic margin in summer compared to winter. However, pronounced zonal positive biases ($\Delta SIT > 1.5$ m) are present in both seasons, particularly along the eastern and northern shelf of the Greenland Sea, the region north of the Canadian Archipelago, and the southern Canadian Basin and Beaufort Sea (Fig. 5c and f).

Considering PIOMAS's known limitations in overestimating thin ice while underestimating thick ice (Laxon et al., 2013; Schweiger et al., 2011), additional validation using CS2SMOS data (Ricker et al., 2017) is conducted (Fig. S1 in the Supplement). Consistent with previous findings, PIOMAS exhibits underestimation in regions with thicker sea ice, such as north of the Canadian Archipelago and east of Greenland (Fig. S1e). Similarly, E3SMv2-MPAS shows pronounced positive biases relative to CS2SMOS in areas including the northern Canadian Archipelago, the southern Canadian Basin, and the Beaufort Sea (Fig. S1d), aligning with the bias pattern identified in comparisons with PIOMAS (Fig. 5c), thereby corroborating the spatial reliability of PIOMAS-indicated biases.

The spatial pattern of maximum positive bias in E3SMv2-MPAS remains consistent across seasons (Fig. 5c and f). This bias is also evident in the model's annual mean SIT distribution relative to PIOMAS (Fig. S2). Previous studies based on CMIP5 models have established a strong correlation between inaccuracies in simulating the Beaufort Gyre and SIT distribution (Stroeve et al., 2014). Since the SSH field serves as a key proxy for evaluating the fidelity of Beaufort Gyre simulations (Wang et al., 2018), we analyze differences in SSH between E3SMv2-MPAS and the ORAS5 reanalysis (Fig. 6a–c). The model overestimates SSH in the Beaufort Sea, suggesting an erroneously enhanced ice convergence. Additionally, the simulated OHC in the 0–100 m layer is underestimated in this region (Fig. 6d–f), which may further contribute to the positive SIT bias. Thus, the persistent 0.5–1 m positive bias in the Beaufort Sea is hypothesized to originate from an overestimated intensity of the Beaufort Gyre and associated upper-ocean thermal biases in E3SMv2-MPAS, which then may impede the realistic export of sea ice through the north of Canadian Archipelago and east of Greenland.

To further analyze long-term trends in sea ice-related variables, including interannual and decadal variability, time series of SIC, SIT, SIE, and SIV are examined over the periods 1960–1980 and 1995–2020 (Fig. 7).

E3SMv2-MPAS successfully reproduces SIC seasonal cycles and interannual variability during 1995–2020, maintaining root mean square errors (RMSE) values of 0.040, 0.052, and 0.051 against NSIDC, Hadley, and ERA5 datasets respectively (Fig. 7a). This validates the dynamic framework's effectiveness in capturing sea ice-atmosphere coupling mechanisms. Trend analysis confirms the model's climate response capability. During the rapid decline period (1995–2020), E3SMv2-MPAS accurately captures accelerated SIC reduction trends, showing better agreement with NSIDC observations than Hadley and ERA5 products. For the weak-trend period (1960–1980), the model reproduces quasi-stable sea ice coverage characteristics. The accelerated SIC decline in the recent period compared to historical decades (1960–1980) highlights the model's ability to replicate trend amplification under intensified forcing, thereby bolstering confidence in its scenario-dependent projections. Similarly, the model effectively captures the interannual and decadal variability of SIE (Fig. 7b; RMSE: 0.96).

Consistent with NSIDC, simulated SIC and SIE exhibit certain seasonal biases. The systematic winter overestimation, attributable to positive SIC biases in the southern Greenland Sea and southward-expanded ice cover in the Barents Sea (Fig. 3e), coinciding with pronounced cold SST biases in these regions (Fig. S3). During summer, E3SMv2-MPAS overestimates the seasonal minimum (Fig. 7a and b), particu-

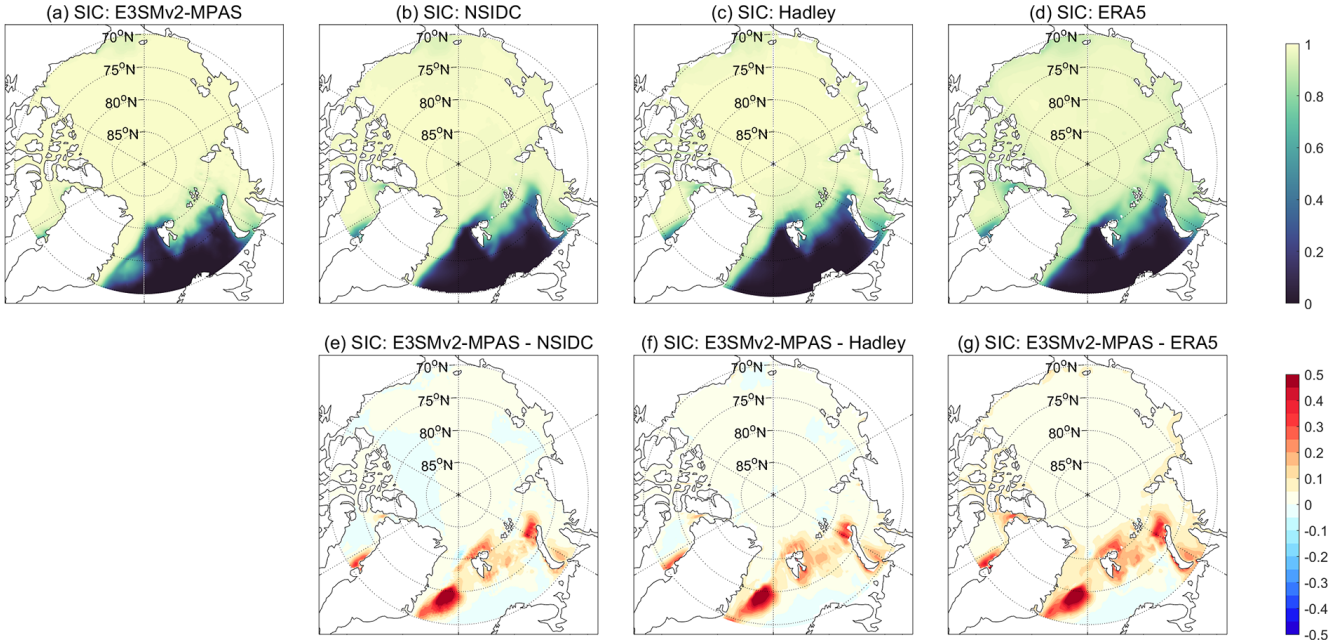

Figure 3. During winter (December–February), **(a–d)** 1995–2020 climatological mean SIC spatial distributions: **(a)** E3SMv2-MPAS simulations, **(b)** NSIDC observational product, **(c)** Hadley Centre HadISST data, **(d)** ERA5 reanalysis. **(e–g)** SIC bias fields: **(e)** E3SMv2-MPAS vs. NSIDC, **(f)** E3SMv2-MPAS vs. Hadley, **(g)** E3SMv2-MPAS vs. ERA5.

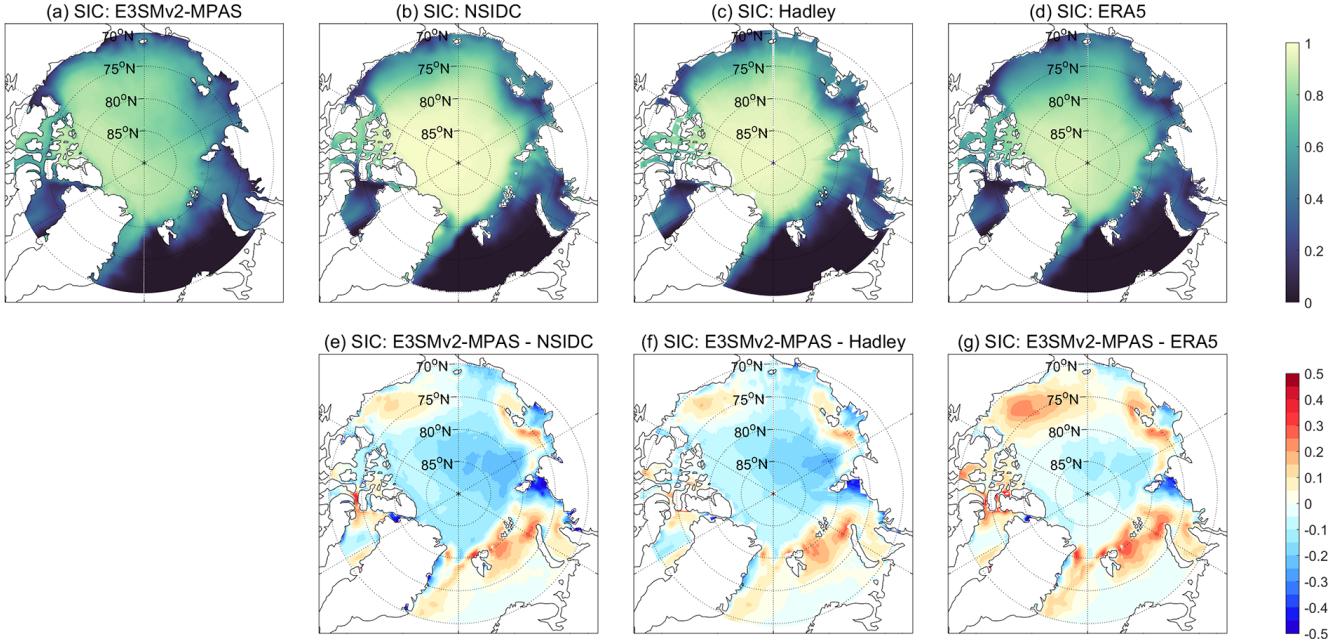

Figure 4. The same as Fig. 3, but during summer (June–August).

larly in the Greenland Sea, Barents Sea, East Siberian-Laptev Seas, and Beaufort Sea (Fig. 4e). These regions also exhibit elevated surface albedo values (Fig. S4), reducing absorbed shortwave radiation and contributing to the sea ice overestimation.

Although the model generally overestimates SIT (Figs. 5 and S2), the time series analysis successfully simulates continuous thinning from ~ 1.8 to ~ 1.3 m during 1995–2020 (Fig. 7c). Notably, however, the simulated thinning rates remain slightly lower than PIOMAS results. Stable RMSE value (~ 0.37) throughout this period confirm ro-

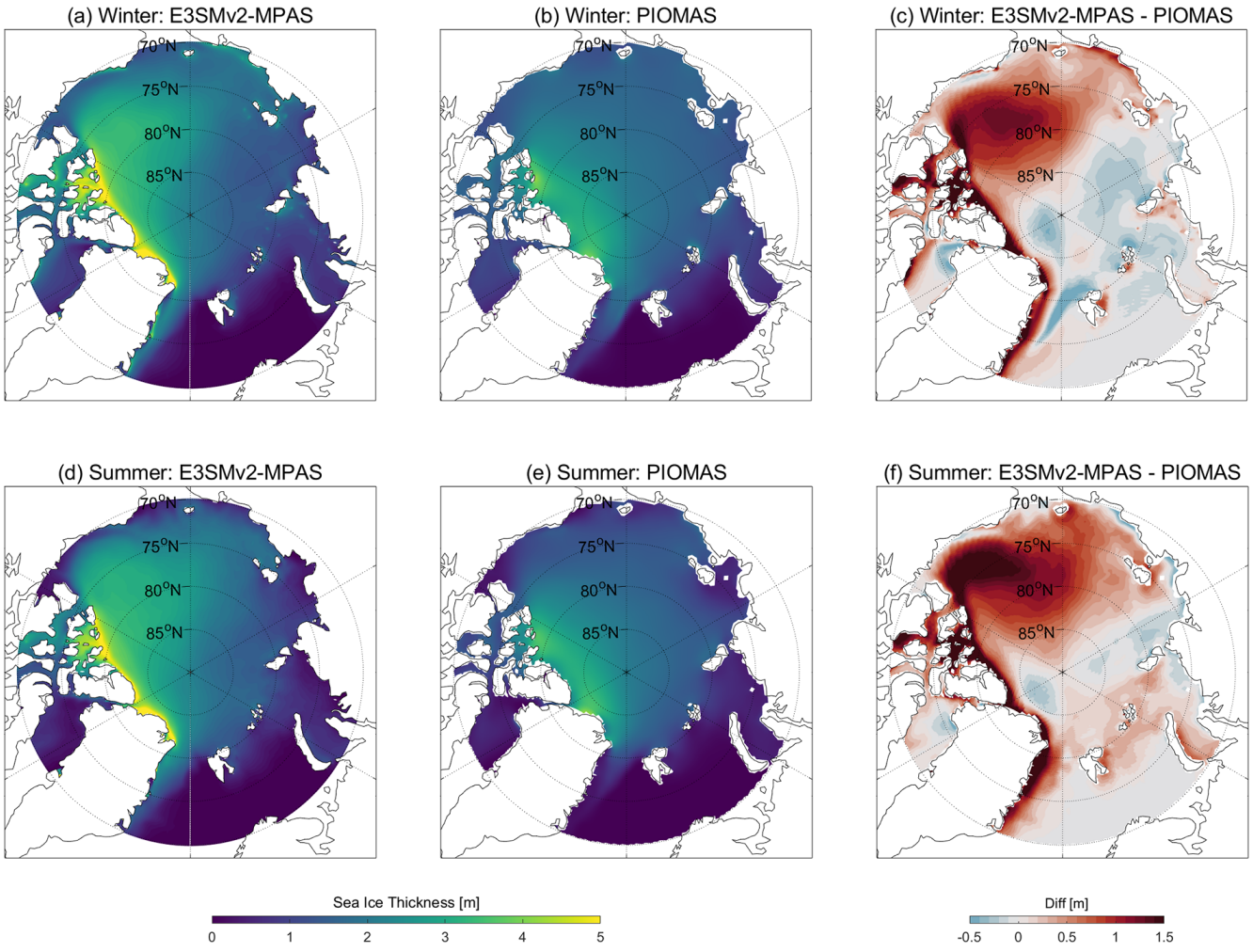

Figure 5. During **(a–c)** winter (December–February) and **(d–f)** summer (June–August), **(a, b, d, e)** 1995–2020 climatological mean SIT spatial distributions: **(a, d)** E3SMv2-MPAS, **(b, e)** PIOMAS. **(c, f)** SIT bias field: E3SMv2-MPAS vs. PIOMAS.

bust simulation of long-term SIT evolution. Similarly, compared to PIOMAS, the simulated SIV is consistently underestimated throughout the period, though the declining trend during 1995–2020 is well captured (Fig. 7d). For the pre-satellite era (1960–1980), evaluation using PIOMAS-20C shows E3SMv2-MPAS reproduces the 6-year cyclic "increase-decrease-increase" SIT fluctuations during 1960–1978 (Fig. 7c). While PIOMAS-20C shows no statistically significant SIT trend during 1960–1980, E3SMv2-MPAS simulates a pronounced thickening trend in this period, potentially linked to its systematic overestimation of regional ice thickness in areas like the Beaufort Sea (Figs. 5c, f and S2c). Nevertheless, across the multi-decadal scale (1960–2020), this coupled system demonstrates a reasonable representation of Arctic SIT and SIV responses to climate forcing.

3.2 Surface thermohaline signatures

SST and SSS engage in complex bidirectional coupling with the atmosphere-ice system through ice/atmosphere-ocean interfacial energy-mass exchange processes. This section evaluates the spatiotemporal co-variability of SST/SSS to elucidate E3SMv2-MPAS's representation of ocean–sea ice–atmosphere interaction mechanisms.

OISST-based validation demonstrates E3SMv2-MPAS accurately reproduces key Arctic SST spatial patterns: (1) temperature gradients decreasing from shelves to central basins, and (2) warm-core features in southern Barents Sea open waters (Fig. 8a–c). Systematic regional biases are identified: the cold biases in the Greenland Sea ($\Delta\mathrm{SST} \approx -2$ to 0 °C) spatially correlate with an overestimation of SIC in the same region, while positive deviations ($\Delta\mathrm{SST} \approx 0$–2 °C) occur near Svalbard's western coast and the Eurasian continental margins. Notably, continental coastal biases are spatially decoupled from Atlantic inflow pathways, with formation mecha-

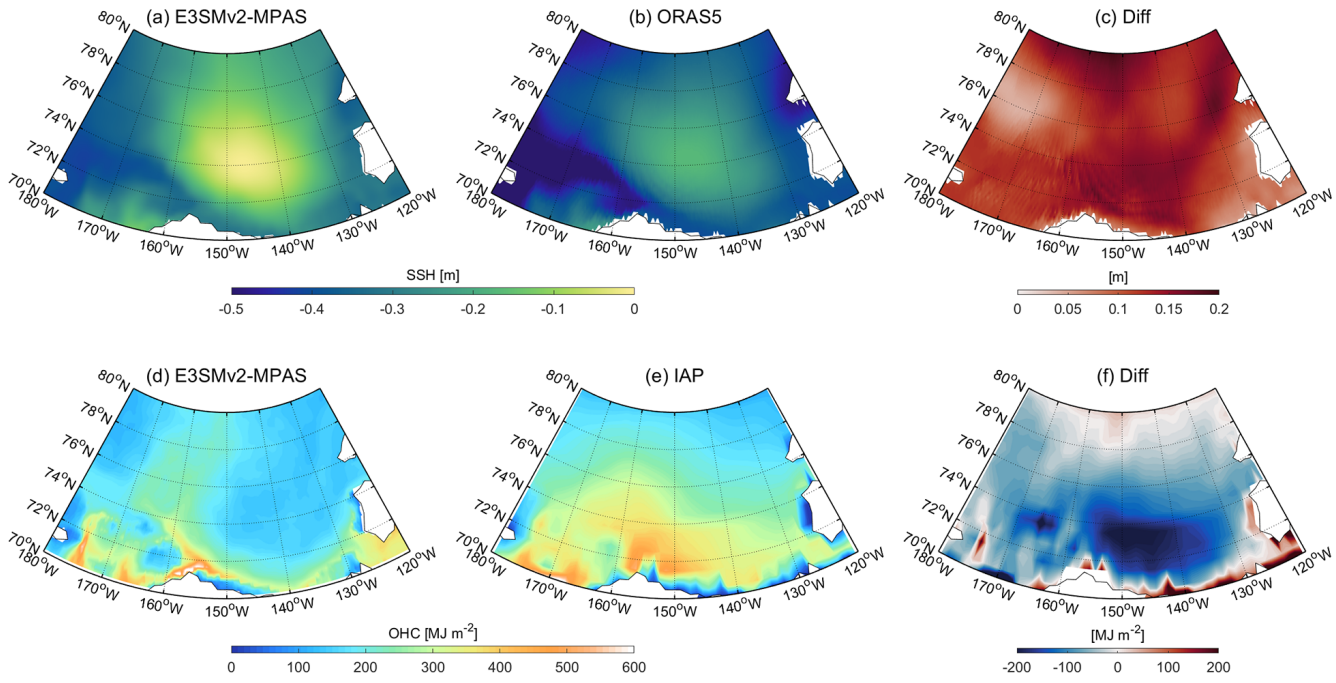

Figure 6. Climatological mean spatial distributions for the period 1995–2020. **(a–c)** SSH: **(a)** E3SMv2-MPAS, **(b)** ORAS5. **(c)** Bias in SSH between E3SMv2-MPAS and ORAS5. **(d–f)** OHC in the upper 100 m: **(d)** E3SMv2-MPAS, **(e)** IAP. **(f)** Bias in OHC between E3SMv2-MPAS and IAP.

nisms likely associated with inaccurate vertical mixing processes stemming from stratification stability biases in shelf regions. E3SMv2-MPAS successfully captures Arctic SST warming trends during the 1995–2020 period, showing high consistency with OISST in accelerated trend characteristics (Fig. 8d). Seasonal cycle and interannual variability simulations remain within acceptable error ranges (RMSE = 0.24), confirming appropriate responses to surface thermal forcing. Furthermore, the model accurately captures both the pronounced SST increase and accelerated decadal warming trend during 1995–2020 relative to the 1960–1980 baseline period. These simulated changes show a strong coupling with the accelerated decline in SIC, SIE, SIT, and SIV concurrently (Fig. 7).

E3SMv2-MPAS demonstrates comparatively weaker performance in SSS simulation versus sea ice and SST variables. Spatially heterogeneous biases are observed: negative deviations ($\Delta SSS = -0$ to 1 PSU) in the Barents and Greenland Seas contrast with pronounced positive biases ($\Delta SSS = 2$–5 PSU) in the Beaufort Sea and the Kara-Beaufort shelf regions (Fig. 9a–c). The 3 PSU overestimation in the Beaufort Sea aligns with advanced assimilation model (such as HYCOM and GLORYS12) biases reported by Hall et al. (2021), suggesting common limitations in Arctic shelf freshwater transport representation. Specifically, inadequate parameterization of surface freshwater budgets and associated processes (e.g., precipitation-evaporation fluxes, river discharge, and ice–ocean interactions) may constrain freshwater cycle simulations (Wang et al., 2024). The Beaufort Sea SIT overestimation identified previously (Fig. 5) potentially exacerbates salinity biases through reduced freshwater release (Kelly et al., 2019). If the intensity of the Beaufort Gyre is overestimated (as discussed in Sect. 3.1), enhanced freshwater retention could impede westward shelf transport to the Kara Sea, potentially driving salinity overestimation in the Kara-Beaufort shelf. Despite spatial biases, E3SMv2-MPAS demonstrates credible simulation of seasonal cycle phasing and amplitude in the Barents Sea SSS, while the temporal variations in the Beaufort Sea show agreement levels comparable to mainstream reanalysis products (Fig. 9d–e; Hall et al., 2021).

In the Greenland and Barents Seas, systematic underestimation of SST and SSS (Figs. 8c and 9c) coincides with overestimation of SIC (Figs. 3 and 4). These regions are situated within the marginal ice zone, where strong surface wind stress facilitates the transfer of energy to deeper ocean layers through the excitation of near-inertial oscillations and associated turbulent mixing processes (D'Asaro, 1985). This discrepancy may be attributed to the model's potential overestimation of this downward energy transfer. Similarly, Zhu et al. (2022) reported that in the equatorial Pacific cold tongue region, the KPP scheme overestimates downward turbulent heat flux, leading to a cold bias in both upper-ocean and sea surface temperatures. A primary reason for these biases lies in the scheme's reliance on a single Richardson number (Ri) relationship for parameterization. Although this approach

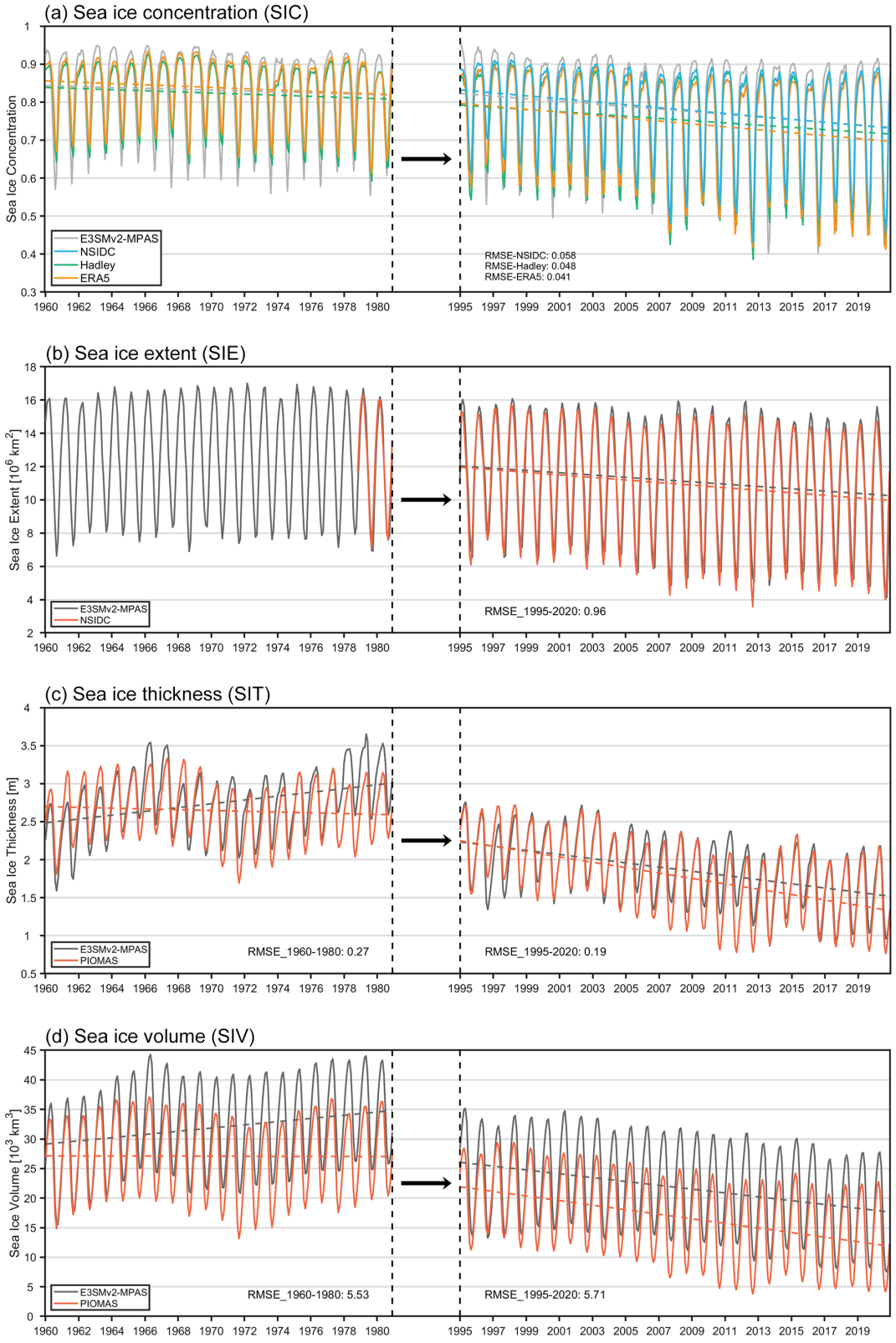

Figure 7. Time series and linear trends of sea ice properties from 1960–1980 and 1995–2020. **(a)** SIC of pan-Arctic (70–90° N) for E3SMv2-MPAS (gray), NSIDC (blue), Hadley (green), and ERA5 (orange). **(b)** SIE for E3SMv2-MPAS (black) and NSIDC (red). **(c)** SIT of pan-Arctic (70–90° N) for E3SMv2-MPAS (black) and PIOMAS (red). **(d)** SIV for E3SMv2-MPAS (black) and PIOMAS (red). Dashed lines denote linear trends based on least-squares regression.

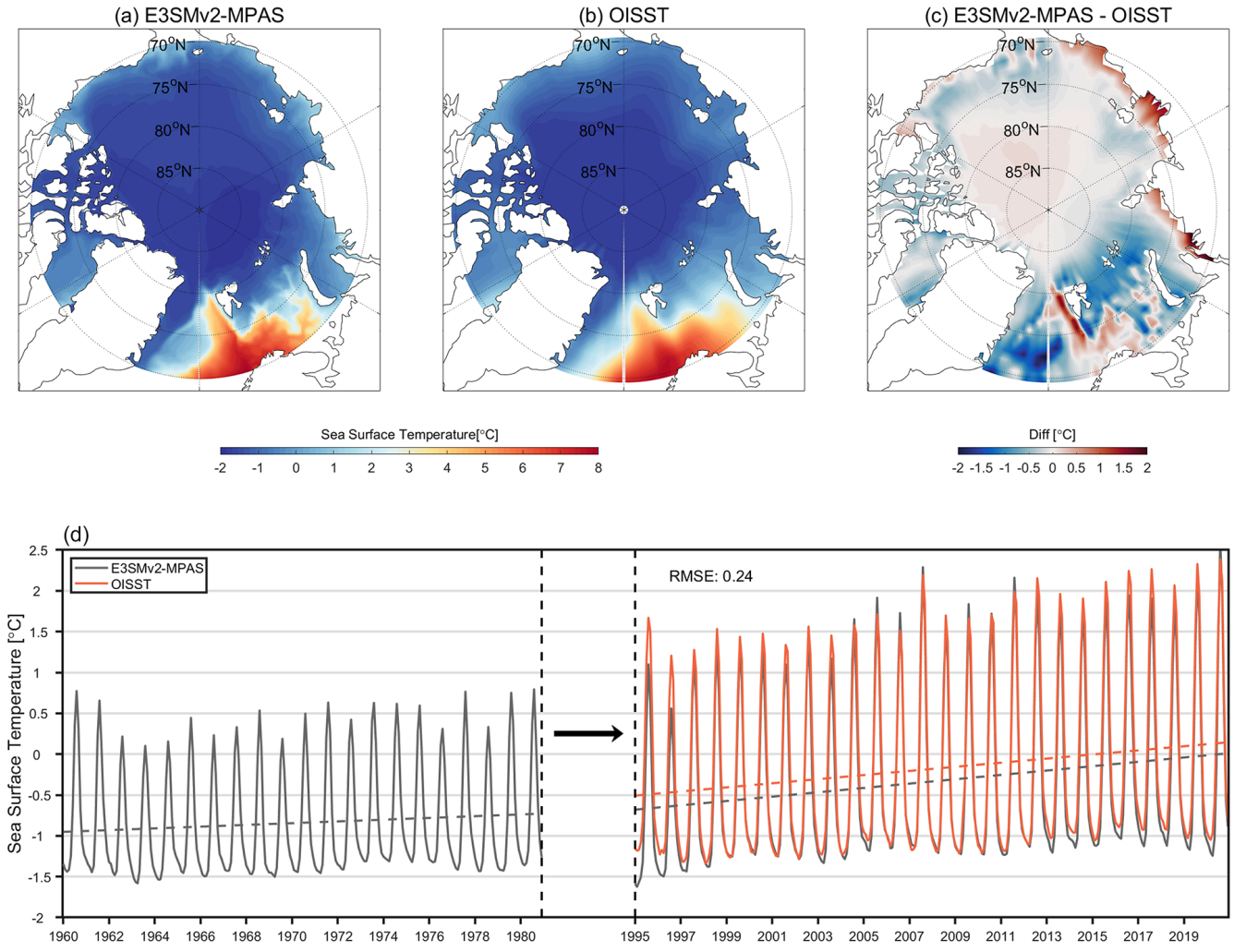

Figure 8. (a, b) 1995–2020 climatological mean SST spatial distributions: **(a)** E3SMv2-MPAS, **(b)** OISST. **(c)** SST bias field: E3SMv2-MPAS vs. OISST. **(d)** Pan-Arctic (70–90° N) mean SST time series for 1960–1980 and 1995–2020, with dashed lines indicating linear trends (E3SMv2-MPAS: black; OISST: red) derived from least-squares regression.

captures instability conditions in stratified shear flows, it is insufficient to uniquely determine turbulent states and mixing intensities (Zhu et al., 2022), thus limiting its performance in complex dynamic environments.

3.3 Three-dimensional thermohaline structure

Accurate simulation of three-dimensional thermohaline fields remains a core technical challenge in ocean model development, directly determining model capability in representing Arctic multi-sphere coupling processes (ocean-ice-atmosphere). While preliminary evaluations of key sea ice properties (including concentration, extent, thickness, and volume) and surface thermohaline diagnostics have validated E3SMv2-MPAS's capacity to simulate Arctic shallow-layer thermal states, subsurface-to-deep thermohaline structure biases may still induce circulation distortions, material transport deviations, cross-basin exchange inaccuracies, and climate feedback misrepresentations. A multi-dimensional verification framework including spatial heterogeneity diagnostics, temporal evolution analysis and three-dimensional dynamical validation is established to assess E3SMv2-MPAS's three-dimensional thermohaline simulation performance comprehensively.

Using the 1995–2014 climatological mean profiles, systematic comparisons are conducted between E3SMv2-MPAS and observational data (Muilwijk et al., 2023) across four regions: the western Eurasian Basin, the eastern Eurasian Basin, the Chukchi Sea, and the Beaufort Sea. Thermohaline profile characteristics (0–1000 m depth) are evaluated through vertical structure evolution and regional variability analyses.

Observational data reveal maximum temperatures (1.6 °C) at 250 m depth in the western Eurasian Basin, decreasing to 0 °C at 800 m (Fig. 10a). E3SMv2-MPAS can successfully

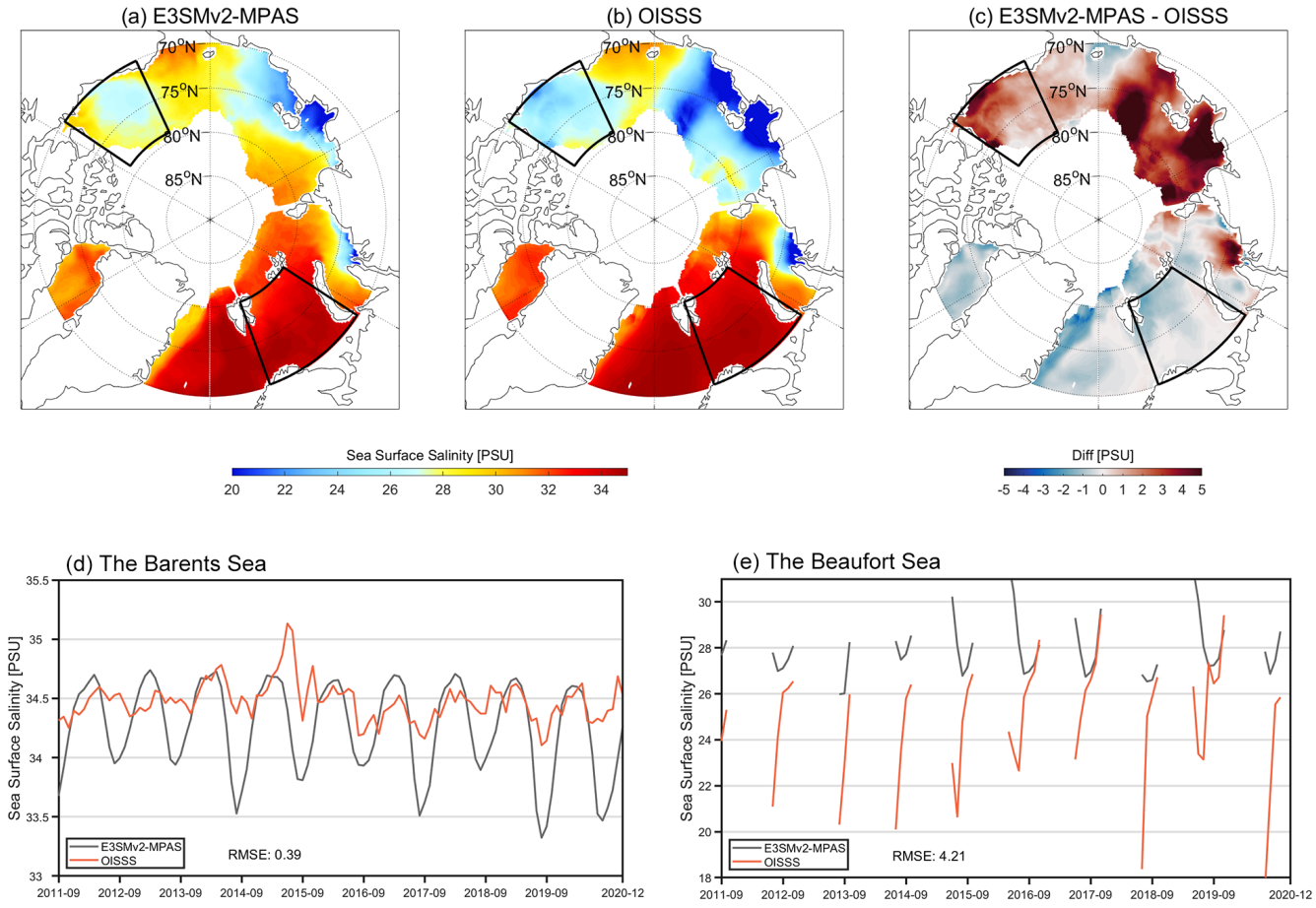

Figure 9. **(a, b)** September 2011–December 2020 climatological mean SSS spatial distributions: **(a)** E3SMv2-MPAS, **(b)** OISSS. **(c)** SSS bias field: E3SMv2-MPAS vs. OISSS. **(d, e)** Regional SSS time series in **(d)** the Barents Sea and **(e)** the Beaufort Sea (black boxes in **a**–**c**; E3SMv2-MPAS: black; OISSS: red).

reproduce observed vertical temperature structure, matching the observed 250 m temperature maximum depth and maintaining temperature decline to 0 °C at 1000 m depth. Despite a ∼ 1 °C core temperature overestimation and 200 m layer thickness bias, its temperature profile RMSE is 0.448.

Observational spatial heterogeneity shows progressive temperature core reductions (1.6 °C → 1.4 °C → 0.8 °C → 0.7 °C) and deepening core depths (250 m → 290 m → 400 m → 420 m) from the western Eurasian Basin to the Beaufort Sea (Fig. 10a–d). E3SMv2-MPAS maintains systematic temperature overestimation (∼ 1° in the western Eurasian Basin, ∼ 0.3° in the Chukchi Sea and the Beaufort Sea) while successfully reproducing spatiotemporal evolution of vertical thermal structures. In salinity simulations, E3SMv2-MPAS demonstrates optimal salinity profile fitting capability through observational agreement starting from 200–300 m depth, as evidenced by the western Eurasian Basin RMSE of 0.204.

In order to systematically assess model capabilities in representing multi-scale Arctic thermal variations, an interdecadal three-dimensional thermohaline evolution framework is established. Depth-time section comparisons between E3SMv2-MPAS and EN.4.2.2 (Good et al., 2013) are conducted to analyze spatiotemporal heterogeneity in Arctic oceanic thermal structures (Fig. 11).

E3SMv2-MPAS successfully reproduces the solar radiation-driven seasonal thermal cycle observed in EN.4.2.2 (Fig. 11). Monthly thermohaline profiles (depth-month coordinates) in the upper 500 m of the Eurasian Basin better illustrate radiation-dominated seasonal characteristics: summer (June–August) surface temperature peaks coincide with salinity minima from meltwater inputs, while winter (December–February) shows sub-freezing temperatures (< -1.8 °C) and salinity recovery (Fig. 12). These core seasonal features are accurately captured, validating high-precision surface flux representation.

E3SMv2-MPAS demonstrates exceptional multi-temporal simulation capabilities for AW dynamics (Fig. 11). Observations reveal stable AW core temperatures (∼ 1.6 °C) during 1960–1980, increasing to ∼ 2 °C in 2000–2020 with core shallowing from 350 to 300 m in the whole Arctic Basin (Fig. 11b). E3SMv2-MPAS accurately reproduces both the

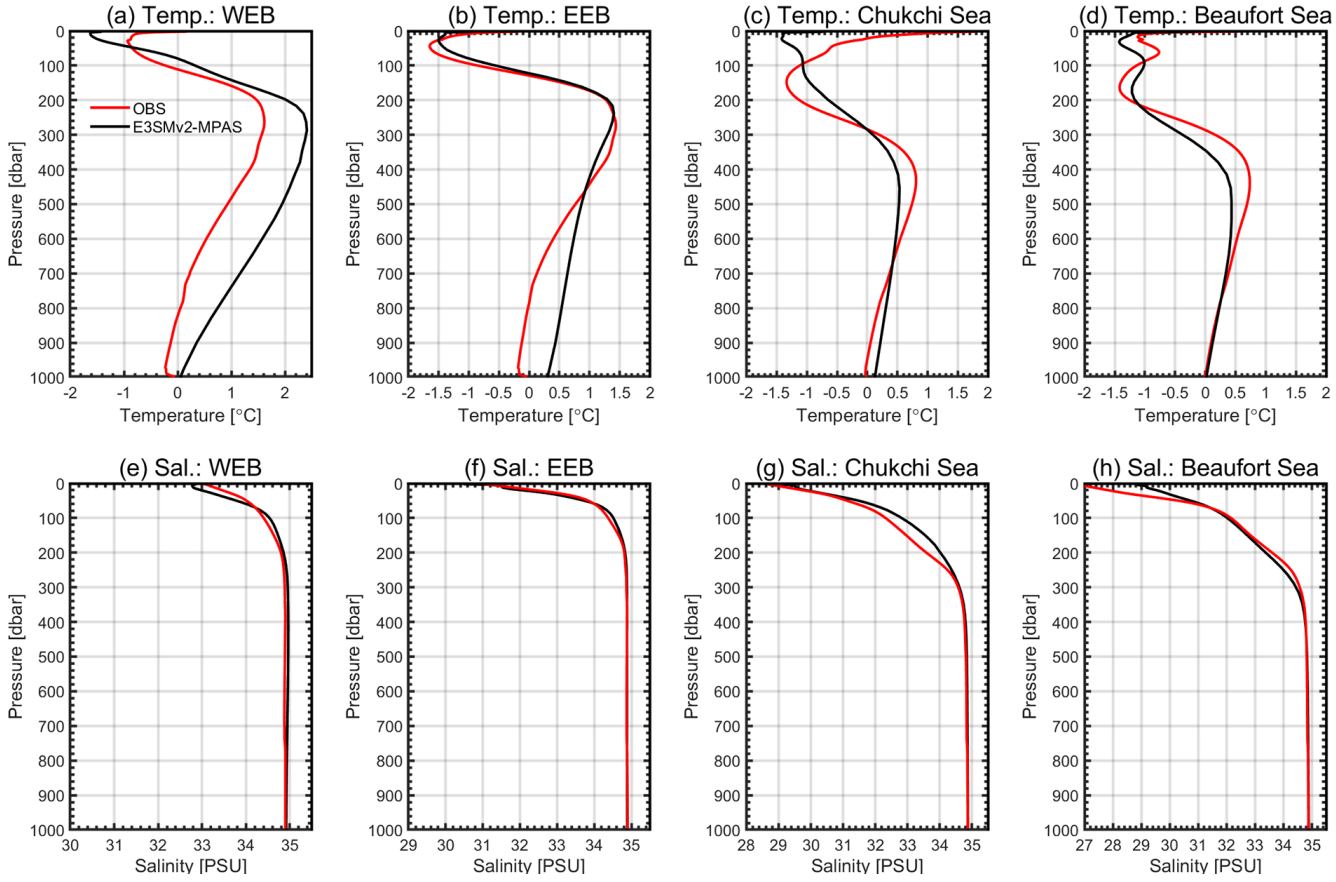

Figure 10. (a–d) 1995–2014 climatological mean temperature profiles from observations (Muilwijk et al., 2023), and E3SMv2-MPAS. **(e–h)** The same as panels **(a)**–**(d)** but for salinity profiles. Basins: the western Eurasian (WEB; **a, e**), the eastern Eurasian (EEB; **b, f**), the Chukchi Sea **(c, g)**, the Beaufort Sea **(d, h)**.

$\sim 0.4\,^{\circ}\mathrm{C}$ warming magnitude and ~ 50 m vertical migration (Fig. 11a). However, regional-specific biases emerge in seasonal variability simulations (Fig. 12). EN.4.2.2 identifies semi-annual signals in the 200–500 m layer of the Eurasian Basin (September–November peaks at $\sim 1.5\,^{\circ}\mathrm{C}$; Fig. 12c), linked to winter Atlantification intensification. E3SMv2-MPAS fails to capture this seasonality, producing persistent warm biases in 200–400 m layers with overestimated spring–summer core temperatures (0.5–0.8 °C; Fig. 12e). This discrepancy may be attributed to the GM parameterization scheme, which models mesoscale eddy effects on heat and salt redistribution through bolus advection and Redi diffusion. In general, the Arctic winter features greater mixed layer depth and weaker stratification due to brine rejection during sea ice formation and wind-driven stirring (Peralta-Ferriz and Woodgate, 2015). These processes promote eddy penetration, increasing the efficiency of vertical heat transport. In contrast, strengthened stratification in summer restricts the vertical scale of eddies and reduces heat transfer. However, the GM scheme employs a fixed diffusion coefficient, which prevents it from capturing the seasonal variability modulated by stratification changes.

We further investigate the decadal-scale thermohaline variability across Arctic basins. The results reveal regional heterogeneity in temperature and salinity trends (Fig. 13). Inter-decadal comparisons (1970s vs. 2000s–2020s; Muilwijk et al., 2023) reveal pan-Arctic synchronous warming across the Eurasian Basin sectors and the Amerasian subregions (Fig. 13e–h). However, E3SMv2-MPAS underestimates the warming in the Amerasian Basin (0.1–0.5 °C biases; Fig. 13c, d, g and h).

In the Eurasian Basin upper layers ($\sim$ 100–450 m; Fig. 13a, b, e and f), observations show dual-mode thermal evolution: shallow warming above temperature cores (100–250 m) contrasts with systematic warming below (250–450 m). Model simulations exhibit spatial heterogeneity: $0.2 \pm 0.1\,^{\circ}\mathrm{C}$ underestimation of shallow warming contrasts with excessive vertical response ranges (250–1000 m vs. observed 250–450 m). Notably, simulated AW layer thickening in the eastern Eurasian Basin during 2000s–2010s lacks observational support (Fig. 13b and f). These discrepancies may be partly attributed to biases in the representation of vertical processes. As indicated by sensitivity experiments such as those of Liang and Losch (2018), enhanced verti-

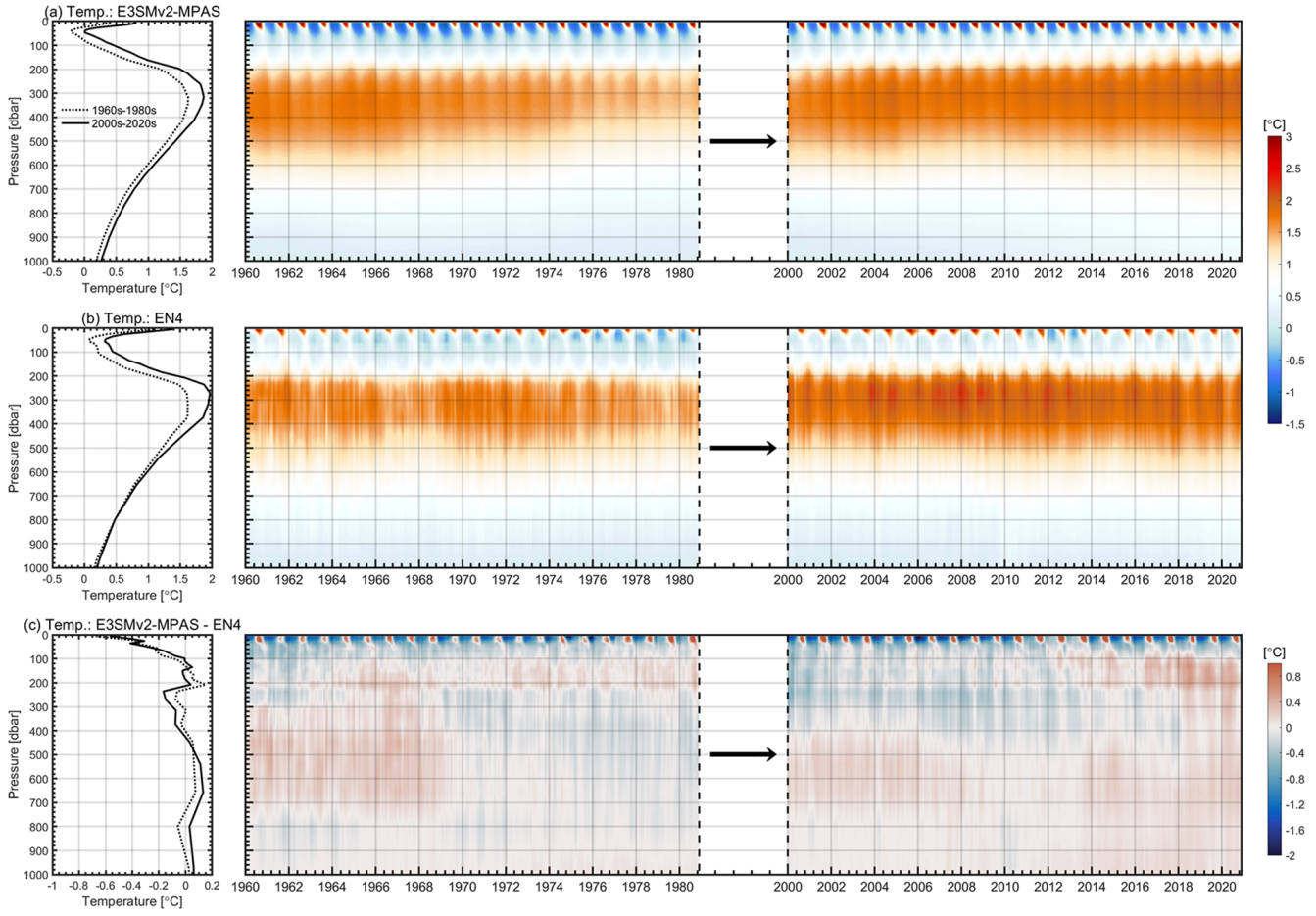

Figure 11. For the Arctic Basin, **(a)** E3SMv2-MPAS simulated temperature profiles (0–1000 m): 1960–1980 climatology (dashed) vs. 2000–2020 climatology (solid). Right: Hovmöller diagram of depth-time evolution (1960–1980 and 2000–2020). **(b)** The same as panel **(a)** but for EN.4.2.2. **(c)** The same as panel **(a)** but for E3SMv2-MPAS minus EN.4.2.2 differences.

cal mixing could promote upward heat transport from AW, potentially causing cooling at intermediate depths (200–900 m). Our model uses a relatively low background diffusivity (1.0×10^{-5} m^2 s^{-1}), which remains constant across time periods despite evidence that Arctic amplification and Atlantification in the 2000s–2010s (Polyakov et al., 2017, 2025; Rantanen et al., 2022; Richards et al., 2022; Shu et al., 2022) may have strengthened vertical mixing compared to the 1970s. The model's failure to represent this temporal increase in mixing efficiency might have limited upward heat transfer, confining warming mainly to intermediate and deeper layers – consistent with the underestimation of shallow warming and exaggerated deep response seen in our simulations.

In the Chukchi Sea, observations indicate basin-wide warming from core layers to AW bottom ($\sim$ 1000 m), showing $\Delta T = 0.2 \pm 0.1$ °C (Fig. 13c, d, g and h). While successfully reproducing Chukchi thermal trends, the model exhibits systematic Beaufort Sea deviations. Salinity changes primarily occur in the upper 300 m of the Amerasian Basin (the Chukchi and Beaufort Seas; observed $\Delta S = -0.3 \pm 0.2$ PSU), with the model failures in capturing the freshening of the Chukchi Sea and underestimation of trends in the shallow-layer (< 80 m) of the Beaufort Sea. The simulated salinity biases may be related to the use of an inappropriately high and constant isopycnal diffusion coefficient ($\kappa = 300$ m^2 s^{-1}) in the GM parameterization. This high diffusion coefficient likely results in excessively strong along-isopycnal mixing, which oversmooths horizontal salinity gradient fronts formed by freshwater accumulation (e.g., from melting ice and increased runoff). During the 1970s, when background freshwater signals were relatively weak, the effect of strong diffusion was less pronounced. However, under the strongly increased freshwater input in the 2000s–2010 (Polyakov et al., 2013; Wang et al., 2019), the persistently high κ value continuously and excessively diffused the simulated upper-layer low-salinity anomalies, hindering their realistic accumulation and maintenance in the basin upper layer. As a result, the model significantly underestimates the magnitude of decadal freshening observed in the region.

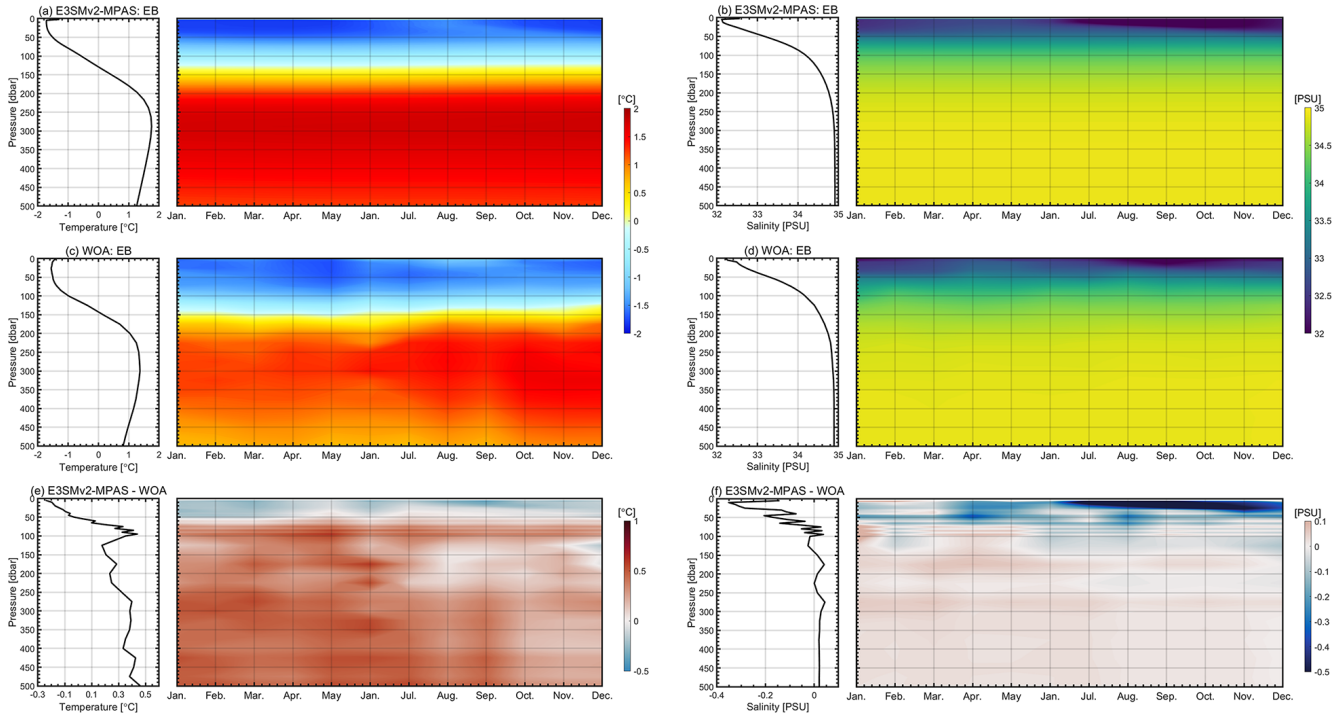

Figure 12. (a, b) E3SMv2-MPAS simulated 1995–2020 climatological mean **(a, c, e)** temperature and **(b, d, f)** salinity profiles (0–500 m) in the Eurasian Basin (EB), with Hovmöller diagrams of monthly variability. **(c, d)** The same as panels **(a)** and **(b)** but for WOA23. **(e, f)** The same as panels **(a)** and **(b)** but for model-observation differences (E3SMv2-MPAS minus WOA23).

AW demonstrates systematic cooling and freshening (temperature and salinity reduction) during its transport from the Eurasian to the Amerasian Basin (Fig. 10), a transformation likely modulated by baroclinic adjustment processes in the inter-basin transition zone. These processes govern cross-basin material-energy exchange (Aksenov et al., 2016). We analyze coordinated meridional sections along 145° W in the Amerasian Basin and 70° E in the Eurasian Basin to access variability in AW properties across space (Fig. 14). WOA23-based comparisons confirm E3SMv2-MPAS's capability in reproducing inter-basin gradient characteristics through three key aspects: (1) AW thermal attenuation: Successful simulation of core temperature decreases from the Eurasian to the Amerasian Basin, replicating thermodynamic dissipation processes; (2) stratification depth displacement: realistic representation of westward-decreasing upper boundary depths matching slope current adjustments; (3) surface freshwater transport effects: accurate reproduction of the surface salinity depression in the Amerasian Basin relative to the Eurasian Basin, validating appropriate parameterization of Pacific-origin freshwater influx mechanisms. Persistent thermal biases in the Eurasian Basin emerge in 145° W sections, with maximum +2 °C warm deviations in 100–500 m core layers (Fig. 14e). Despite absolute temperature biases, maintained meridional heat transport gradients confirm fundamental physical framework validity for large-scale advection processes.

3.4 Freshwater content spatiotemporal variability

The Arctic Ocean constitutes a major freshwater reservoir within the global climate system. Since the mid-1990s, the freshwater content (FWC) in the Arctic Ocean has exhibited a marked increasing trend, primarily driven by persistent anticyclonic atmospheric forcing over the Beaufort Gyre region (1997–2018) and the reduction of Arctic sea ice (Proshutinsky et al., 2019; Wang et al., 2024). This excess freshwater is exported into the North Atlantic through Fram Strait and Davis Strait (Wang et al., 2019), eventually reaching convection regions in the Labrador and Greenland–Iceland–Norwegian Seas. These areas are critical for the formation of global deep waters, which act as a key driver of large-scale ocean circulation systems, including the Atlantic Meridional Overturning Circulation (AMOC) (Arzel et al., 2007). The southward transport of freshwater may influence circulation dynamics by reducing seawater density and suppressing vertical mixing (Haine et al., 2023). Furthermore, Arctic freshwater variability significantly influences ecosystem structure and function (Proshutinsky et al., 2019). Therefore, accurately assessing the freshwater content in the Arctic Ocean represents a central challenge in physical oceanography and climate dynamics, with major implications for understanding both climate variability and long-term change (Haine et al., 2023).

The FWC is defined as follows (Wang et al., 2024):

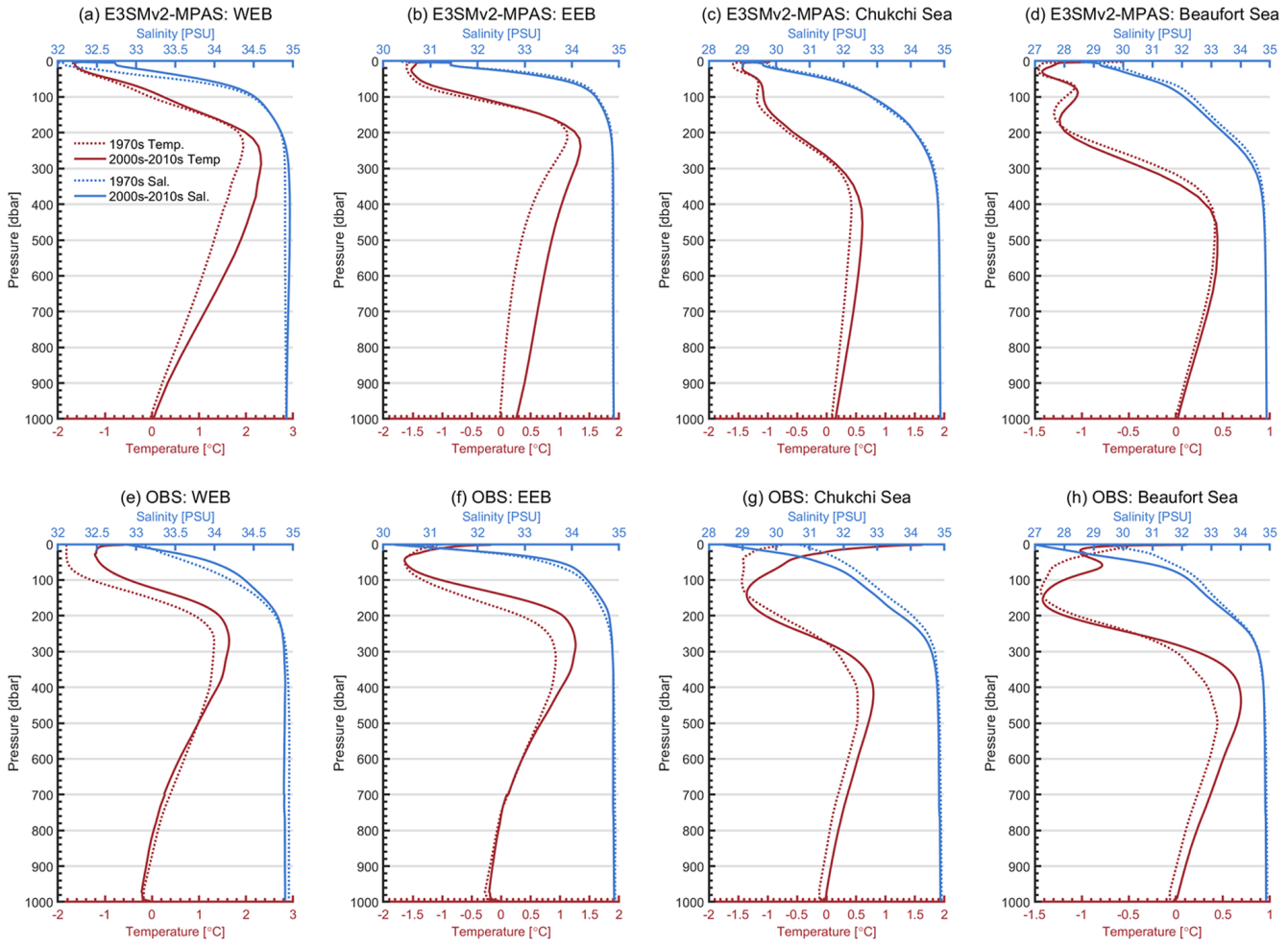

Figure 13. (a–d) Vertical profiles of climatological mean temperature (red curves) and salinity (blue curves) in the western Eurasian Basin (WEB; **a**), the eastern Eurasian Basin (EEB; **b**), the Chukchi Sea **(c)**, and the Beaufort Gyre **(d)** from E3SMv2-MPAS: dashed lines denote 1970s (1971–1979), solid lines represent 2000s–2010s (2001–2019). **(e, f)** Corresponding observational profiles from Muilwijk et al. (2023) with identical temporal averaging.

$$\mathrm{FWC} = \int_{H}^{0} \frac{S_{\mathrm{ref}} - S}{S_{\mathrm{ref}}} \mathrm{d}z, \tag{1}$$

where S denotes salinity, S_{ref} is the reference salinity – set to 34.8 psu, the mean Arctic Ocean salinity according to Aagaard and Carmack (1989) – and H represents the depth at which salinity equals S_{ref}.

Based on this formulation, we evaluate the spatial distribution of the multi-year mean (1995–2020; Fig. 15a and b) and decadal differences (2005–2014 vs. 1995–2004; Fig. 15c and d) of FWC as simulated by E3SMv2-MPAS, in comparison with observational data from WOA23. Additionally, we analyze the basin-wide averaged time series of FWC across the Arctic Ocean (Fig. 15e).

As shown in Fig. 15a and b, E3SMv2-MPAS generally captures the spatial characteristics of Arctic FWC, such as the increase from the Eurasian Basin toward the Amerasian Basin and the maximum values located in the Beaufort Sea. However, the model overestimates FWC in the vicinity of Baffin Bay.

Observational results from WOA23 indicate a pronounced strengthening of FWC in the Beaufort Sea during 2005–2014 compared to 1995–2004. The model successfully reproduces this decadal change in that area (Fig. 15c and d). Nonetheless, E3SMv2-MPAS erroneously simulates a significant decrease in FWC across the Eurasian and Makarov Basins, where WOA23 shows a slight increase. Moreover, the model overestimates the increase in FWC along a pathway extending from the east of Greenland to the northern Canadian Archipelago and into the Canada Basin.

The time series of the total Arctic FWC (Fig. 15e) exhibits a fluctuating upward trend from 1995 to 2020. Polyakov et al. (2013) reported a notable acceleration in Arctic FWC accumulation during the 2000s, particularly between 2003

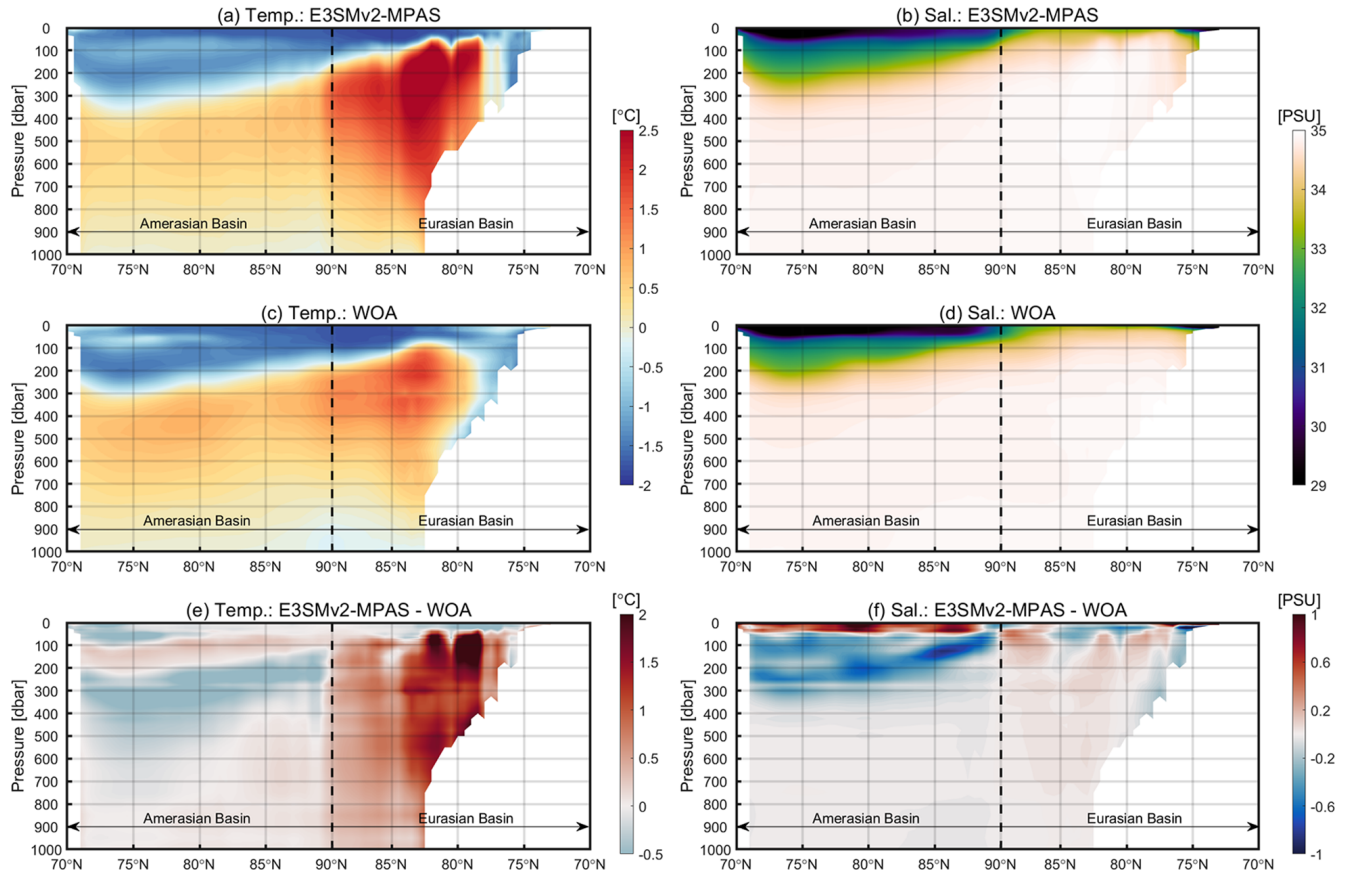

Figure 14. **(a, b)** E3SMv2-MPAS simulated 1995–2020 climatological **(a, c, e)** temperature and **(b, d, f)** salinity distributions along the 145° W–70° E transect (location mapped in Fig. 1b). **(c, d)** The same as panels **(a)** and **(b)** but for WOA23. **(e, f)** The same as panels **(a)** and **(b)** but for the model-observation differences (E3SMv2-MPAS minus WOA23).

and 2010 – a trend that aligns with the sharp rise simulated by E3SMv2-MPAS between 2002 and 2008. Furthermore, Wang et al. (2019) noted a levelling off of the FWC growth trend after 2010, which is also captured by the model.

3.5 Gateway transports: volume, heat, and freshwater

Over the past decades, the Arctic climate system has undergone rapid changes, including shifts in sea ice, atmosphere, and ocean conditions (Landrum and Holland, 2020; Polyakov et al., 2005; Shu et al., 2022). These rapid changes are closely linked to the lateral exchanges of heat and freshwater across the boundaries of the Arctic (Von Schuckmann et al., 2020). The Arctic Ocean's connections to other oceans are defined by four major gateways (from east to west): Bering Strait, Fram Strait, Barents Sea Opening, and Davis Strait (Tsubouchi et al., 2024). These critical gateways not – as discussed in the previous section – serve as major pathways for freshwater export from the Arctic, which in turn influences global deepwater formation, large-scale circulation, and ecosystems, but also subject Arctic sea ice and ocean conditions to strong influences from Atlantic and Pacific water inflows. These impacts include modulating sea ice cover (Årthun et al., 2012, 2019; Docquier and Koenigk, 2021), ocean stratification (Veneziani et al., 2022), ecosystem (Woodgate and Peralta-Ferriz, 2021), ocean temperature (Barton et al., 2018), and freshwater content (Woodgate, 2018). Therefore, the accurate simulation of volume, heat, and freshwater transports through these four major gateways – including their interannual and decadal variability – is crucial. In this section, we evaluate the performance of the E3SMv2-MPAS in simulating these key exchanges through comparison with multi-source observational data.

The oceanic net volume transport (VT), heat transport (HT), and freshwater transport (FWT) through the key gateways – Bering Strait, Fram Strait, Barents Sea Opening, and Davis Strait – are calculated as follows (Karpouzoglou et al., 2022; Shu et al., 2022; Wang et al., 2024):

$$\mathrm{VT} = \int_{-H(\lambda)}^{0} \int_{\lambda_1(z)}^{\lambda_2(z)} V \mathrm{d}\lambda \mathrm{d}z, \tag{2}$$

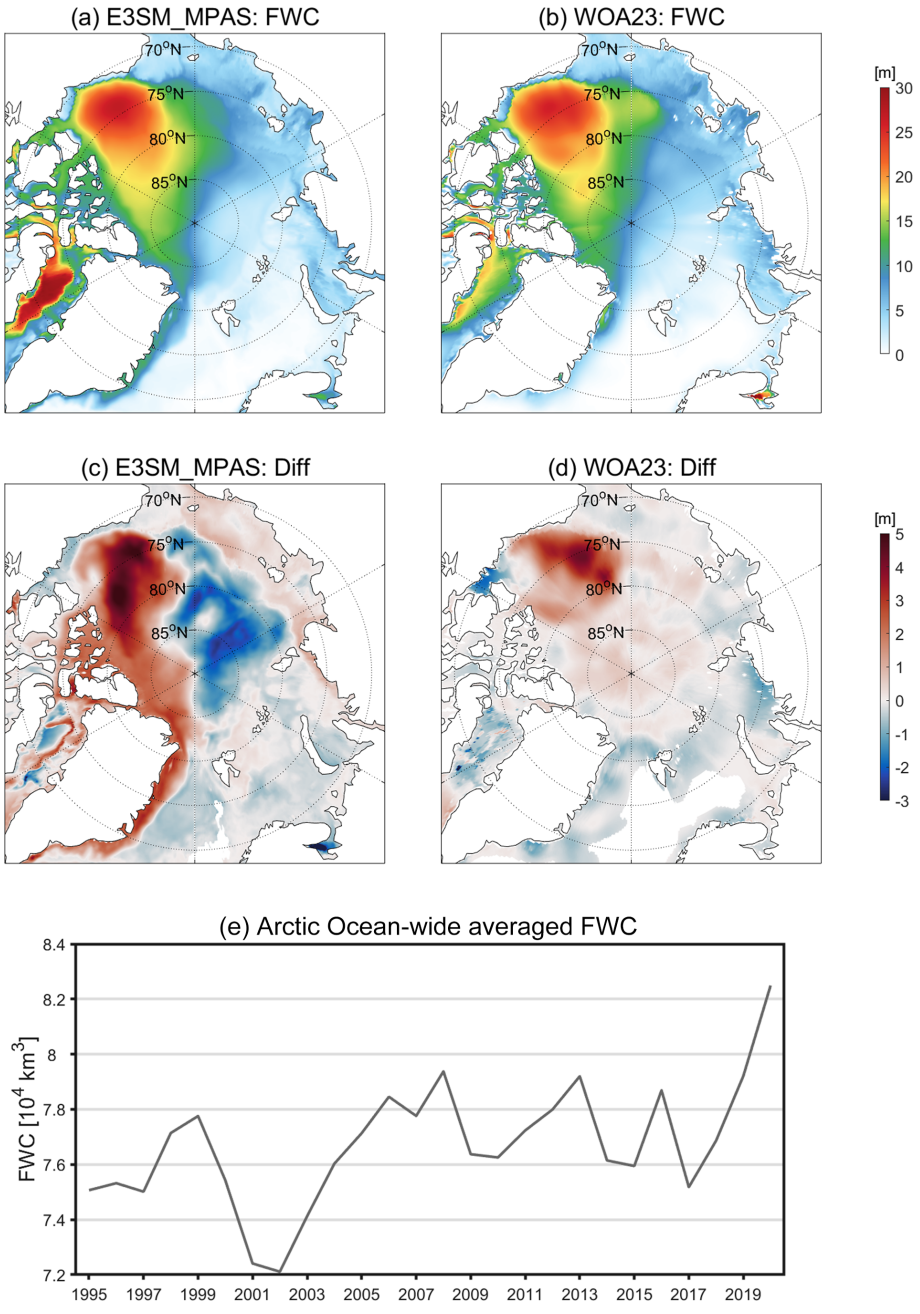

Figure 15. Spatial distribution and temporal evolution of FWC (in meters) in the Arctic Ocean. **(a, b)** Multi-year mean (1995–2020) FWC from **(a)** E3SMv2-MPAS and **(b)** WOA23. **(c, d)** Decadal difference in FWC (2005–2014 minus 1995–2004) from **(c)** E3SMv2-MPAS and **(d)** WOA23. **(e)** Time series of the Arctic Ocean-wide averaged FWC from E3SMv2-MPAS for the period 1995–2020.

$$\mathrm{HT} = \rho_o c_p \int_{-H(\lambda)}^{0} \int_{\lambda_1(z)}^{\lambda_2(z)} V\,(T - T_{\mathrm{ref}})\,\mathrm{d}\lambda\mathrm{d}z, \tag{3}$$

$$\mathrm{FWT} = \int_{-H(\lambda)}^{0} \int_{\lambda_1(z)}^{\lambda_2(z)} V \frac{(S_{\mathrm{ref}} - S)}{S_{\mathrm{ref}}} \mathrm{d}\lambda\mathrm{d}z. \tag{4}$$

Here, V, T, and S denote velocity, potential temperature, and salinity, respectively; ρ_o is the seawater density; and c_p represents the specific heat capacity of seawater. The reference temperature T_{ref} is set to 0 °C, and the reference salinity S_{ref} is defined as 34.8, corresponding to the mean salinity of the Arctic Ocean (Aagaard and Carmack, 1989). The integration is performed over the full depth H – defined as the bathymetry along the transect – and across the lateral ex-

tent λ of each strait. Units for VT, HT, and FWT are Sverdrup (Sv; $1\,\mathrm{Sv} = 10^6\,\mathrm{m^3\,s^{-1}}$), Terawatt (TW), and $\mathrm{km^3\,yr^{-1}}$, respectively.

3.5.1 Bering Strait

Observational data from the Bering Strait between 2000 and 2018 (Woodgate and Peralta-Ferriz, 2021) reveal significant increasing trends in volume, heat, and freshwater transports (Fig. 16a–c). However, E3SMv2-MPAS fails to reproduce these overall trends. The discrepancies in volume and freshwater transports may be attributed to biases in the JRA55 reanalysis and river runoff forcing data (Wang et al., 2024). Although the model does not capture the increasing trends in volume and freshwater transports during 2000–2012, it successfully simulates the upward trends from 2012 to 2018, including interannual variability, with deviations generally within 0.2 Sv and $500\,\mathrm{km^3\,yr^{-1}}$ (Fig. 16a and c). The similar interannual and decadal variability between simulated volume and freshwater transports indicates that the model accurately represents the mechanism whereby increased freshwater transport is primarily driven by volume transport (Woodgate and Peralta-Ferriz, 2021). For heat transport, the model also captures the rapid increasing trend observed after 2012 (Fig. 16b).

3.5.2 Fram Strait

A study by Schauer et al. (2004) shows annual mean net volume transport through the Fram Strait between -4 ± 2 and -2 ± 2 Sv during 1997–2000. Schauer et al. (2008) further indicate values of -2 ± 5.9 Sv (1997–2002) and -2 ± 2.7 Sv (2002–2006). Despite considerable uncertainties in observations, these estimates confirm that the simulated volume transport by E3SMv2-MPAS falls within a plausible range (Fig. 16d). Results from Tsubouchi et al. (2024) for 2005–2009 show that, although the model generally overestimates southward volume transport, it reproduces the interannual variability reasonably well (Fig. 16d). Observations indicate that the annual mean net heat transport increased from 16 ± 12 TW in 1997 to 41 ± 5 TW in 1999 (Schauer et al., 2004). In comparison, the model overestimates heat transport in 1997 but accurately captures both the pronounced increasing trend during 1997–1999 and the value in 1999 (Fig. 16e). Compared to observational data from 2005–2009 (Tsubouchi et al., 2024), the simulated heat transport values agree well in magnitude, and the model largely reproduces the initial decrease followed by an increase during this period. Moreover, the model successfully captures both the increasing trend and the magnitude of the observed southward freshwater transport through the Fram Strait from 2004 to 2017 (Karpouzoglou et al., 2022; Fig. 16f).

3.5.3 Barents Sea opening

Between 2000 and 2009, the annual mean net volume and heat transports through the Barents Sea Opening were reported as 2.3 Sv and 70 ± 5 TW, respectively (Smedsrud et al., 2013), which are generally consistent with the model simulations (Fig. 16g and h). E3SMv2-MPAS also successfully reproduces the decreasing trends in both volume and heat transport during 2005–2008, albeit with slight systematic overestimation. Observations indicate a pronounced decreasing trend in freshwater export through the Barents Sea Opening during 2005–2009 (Tsubouchi et al., 2024). While the model captures this trend, it overestimates the magnitude (Fig. 16i). Additionally, the mean freshwater transport through the Barents Sea Opening between 2000 and 2010 was $-90 \pm 90\,\mathrm{km^3\,yr^{-1}}$ (Haine et al., 2015), further supporting the model's tendency to overestimate freshwater export in this region.

3.5.4 Davis Strait

Observations from 2004 to 2010 report annual mean net volume and freshwater transports through the Davis Strait as -1.6 ± 0.5 Sv and $-2900 \pm 190\,\mathrm{km^3\,yr^{-1}}$, respectively (Curry et al., 2014). E3SMv2-MPAS simulations agree well with these values during the same period (Fig. 16j and l). The model accurately captures the increased freshwater export through the Davis Strait in the mid-to-late 2010s (particularly 2015–2017), which is influenced by Arctic-external atmospheric forcing affecting sea level variability (Wang et al., 2022; Fig. 16l). According to Wang et al. (2022), the freshwater export through the Davis Strait increased by over $1500\,\mathrm{km^3\,yr^{-1}}$ between 2010 and 2017, a magnitude quantitatively reproduced by E3SMv2-MPAS. However, the simulated heat transport ranges from 13 to 19 TW during 2005–2009, underestimating the observed range of 19–27 TW (Tsubouchi et al., 2024; Fig. 16k).

4 Atlantic water layer states

4.1 Parametric characterization of Atlantic water core

As demonstrated in Sect. 3, model biases predominantly manifest in two critical parameters: AW core temperature (AWCT) and depth (AWCD). These metrics, defined as the maximum temperature within 150–900 m depth and its corresponding depth (Khosravi et al., 2022; Shu et al., 2022; Wang et al., 2024), are employed to evaluate E3SMv2-MPAS's performance in reproducing spatiotemporal features of AW (Fig. 17). Observational AWCT/AWCD datasets from Richards et al. (2022) reveal successful model reproduction of baseline spatial gradients: decreasing AWCT and increasing AWCD from the Eurasian to the Amerasian Basin, though with marked regional heterogeneity (Fig. 17a–d). Systematic overestimation of AWCT (+0.5 °C) is identified

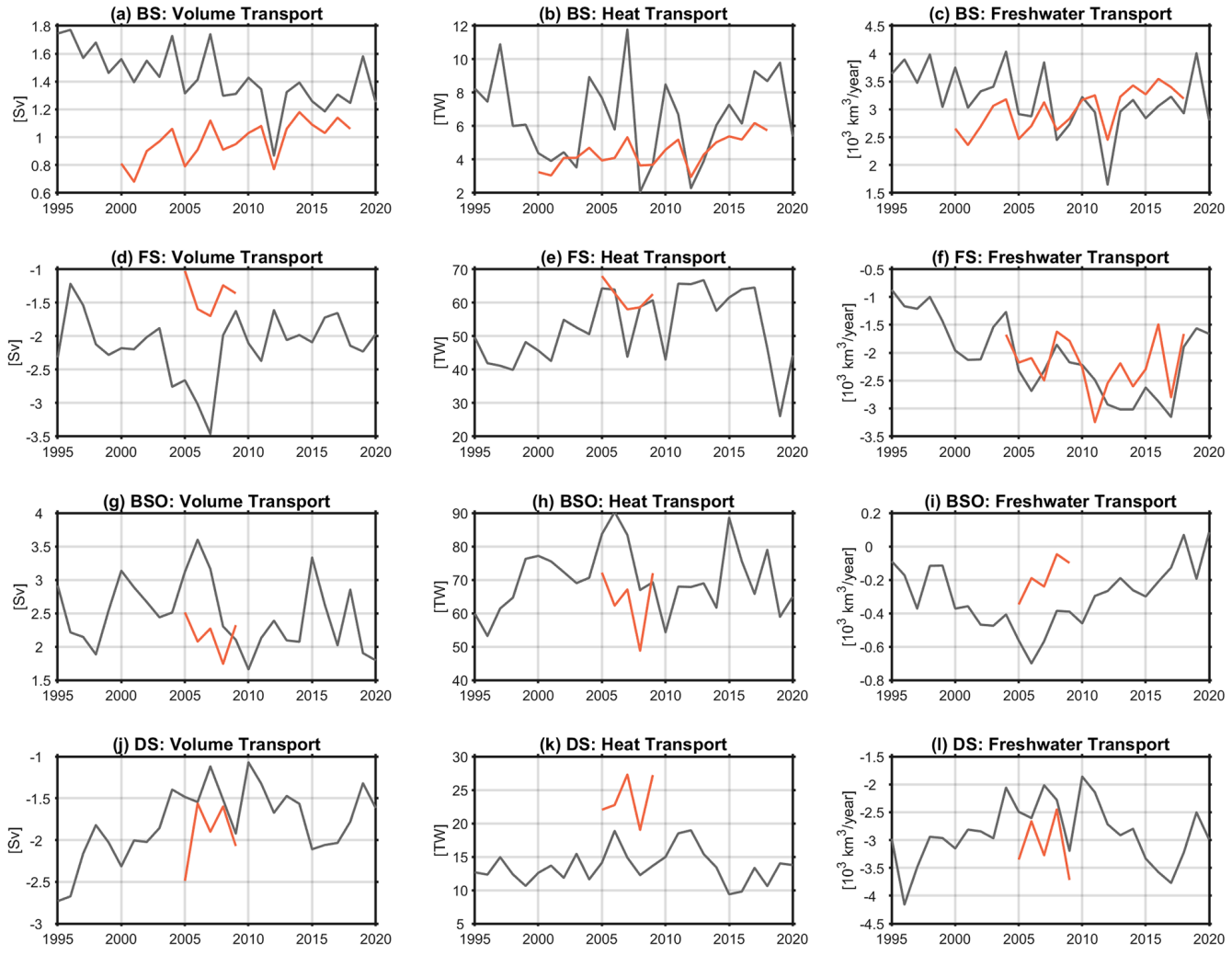

Figure 16. Time series of net **(a, d, g, j)** volume, **(b, e, h, k)** heat, and **(c, f, i, l)** freshwater transport through the **(a–c)** Bering Strait (BS), **(d–f)** Fram Strait (FS), **(g–i)** Barents Sea Opening (BSO), and **(j–l)** Davis Strait (DS) from 1995 to 2020. Black and red lines denote simulated results from E3SMv2-MPAS and observational estimates, respectively. Positive values represent transport into the Arctic Ocean, while negative values denote transport out of the Arctic Ocean. Observational data are from Woodgate and Peralta-Ferriz (2021) for BS; Tsubouchi et al. (2024) for volume and heat transport in FS; Karpouzoglou et al. (2022) for freshwater transport in FS; and Tsubouchi et al. (2024) for BSO and DS. The locations of the four straits are highlighted in green in Fig. 1b.

in the western Eurasian Basin off-shelf regions (high-latitude sectors), while negative deviations ($-0.5\,^{\circ}\mathrm{C}$) occur in the Beaufort Sea. AWCD simulations demonstrate higher accuracy, with minor underestimation ($\Delta Z < 100\,\mathrm{m}$) in the eastern Eurasian Basin.

Interannual variability (1995–2018) is adequately captured through basin-averaged AWCT/AWCD magnitudes (Fig. 17e and f). However, post-2013 increases in AWCD in the Amerasian Basin remain unresolved. While demonstrating credibility in long-term trend simulations, model responsiveness to decadal-scale climatic shifts requires further optimization – critical for predicting nonlinear Atlantification trajectories.

To address the systematic underestimation of Atlantification in model simulations (mentioned in Sect. 1), five key parameters are quantified: AWCT, AWCD, AW upper boundary ($0\,^{\circ}\mathrm{C}$ isotherm; Meyer et al., 2017), AW layer thickness (between $0\,^{\circ}\mathrm{C}$ isotherms), and AW heat content. By analyzing their spatiotemporal response characteristics, this study investigates the trans-decadal evolution of Atlantification.

The AW heat content is calculated as follows (Polyakov et al., 2017):

$$Q = \int_{z_1}^{z_2} \rho_{\mathrm{w}} c_{\mathrm{p}} \left(\theta - \theta_{\mathrm{freezing}}\right) \mathrm{d}z \tag{5}$$

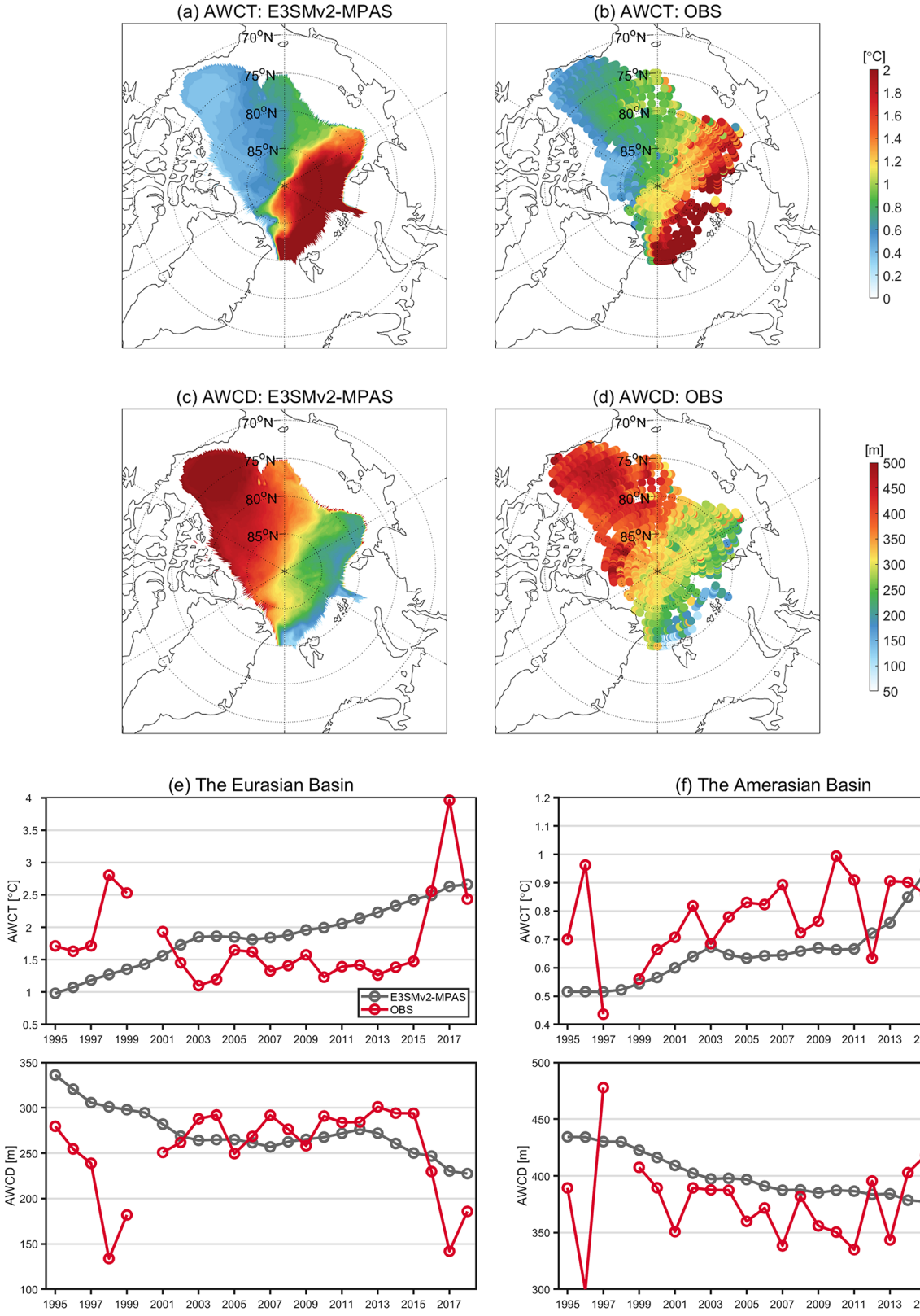

Figure 17. **(a, b)** 1995–2018 climatological mean AWCT spatial distributions: **(a)** E3SMv2-MPAS vs. **(b)** observation from Richards et al. (2022). **(c, d)** The same as panels **(a)** and **(b)** but for AWCD. **(e, f)** Temporal evolution of basin-averaged AWCT (top row) and AWCD (bottom row) in the Eurasian Basin **(e)** and the Amerasian Basin **(f)**: E3SMv2-MPAS (black) versus observations (red).

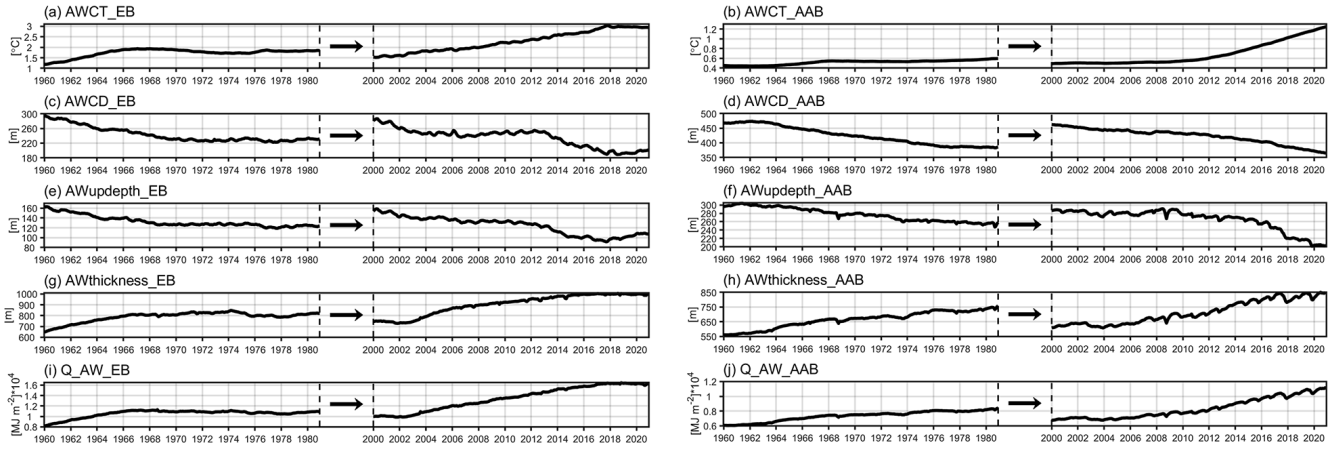

Figure 18. (a, b) 1960–1980 vs. 2000–2020 climatological mean AWCT in the **(a)** Eurasian basin (EB) and **(b)** Amerasian Basin (AAB). **(c–j)** The same as panels **(a)** and **(b)** but for AWCD **(c, d)**, AW layer upper boundary depth (AWupdepth; **e, f**), thickness (AWthickness; **g, h**), and heat content (Q_AW; **i, j**).

where z_1/z_2 denote layer boundaries, ρ_w seawater density, c_p specific heat of seawater, and $\theta_{freezing}$ freezing temperature.

Both basins exhibit coordinated changes during 1960s–1980s and 2000s–2020s: AWCT increases, AWCD decreases, AW upper boundary shallows, layer thickness expands, and heat content accumulates (Fig. 18). Post-2000s acceleration of these trends shows tight coupling with enhanced Atlantic meridional heat transport under Arctic amplification. E3SMv2-MPAS captures the key thermodynamic signatures of Atlantification (the Eurasian Basin vs. the Amerasian Basins between 2000–2020), aligning closely with observationally derived mechanisms of AW intrusion and its climatic impacts (Polyakov et al., 2017): (1) a 1 °C gradient in AWCT between the Eurasian and Amerasian Basins, consistent with zonal heat dissipation; (2) a 130 m shallower AWCD in the Eurasian Basin, reflecting intensified vertical mixing due to sea ice loss; (3) synergistic changes in AW layer thickness and heat content (100 m thinner layer with $+4000\,MJ\,m^{-2}$ in the Eurasian Basin), confirming advective-diffusive redistribution.

This multi-scale validation confirms E3SMv2-MPAS's physical credibility in reproducing Atlantification mechanisms: cascading heat flux-stratification-heat content responses and inter-basin thermodynamic evolution. The model thus provides critical process fidelity for predicting Arctic oceanic thermal threshold transitions.

4.2 Coupling between the Atlantic water and surface layers

The AW layer constitutes the most critical oceanic heat reservoir in the Arctic Ocean (Carmack et al., 2015), containing sufficient thermal energy to melt all Arctic sea ice within several years (Turner, 2010) and capable of dissolving 3–4 times the current ice volume (Carmack et al., 2015; Polyakov et al., 2020b). A pronounced halocline characterized by rapidly increasing salinity with depth typically separates the cold, low-salinity surface waters from the warm, saline AW in the Eurasian and Amerasian Basins. This strong stratification effectively inhibits vertical water mass exchange (Peralta-Ferriz and Woodgate, 2015), isolating the AW layer from sea ice and mixed layer interactions (Aagaard et al., 1981; Richards et al., 2022). Under these physical constraints, vertical heat transport primarily occurs through molecular-scale processes involving internal wave breaking and double-diffusive mixing (Davis et al., 2016). However, since the 1970s, progressive weakening of the eastern Eurasian Basin halocline has been documented (Polyakov et al., 2010; Steele and Boyd, 1998), culminating in its complete failure as an effective thermal barrier for intermediate AW heat by the mid-2010s (Polyakov et al., 2020a). Stratification collapse has triggered a regime shift from double-diffusive dominance to shear-driven turbulent mixing, fundamentally altering vertical heat flux dynamics (Polyakov et al., 2020a).

The KPP scheme employed by E3SMv2-MPAS driven by Gradient Ri physics (Zhu et al., 2022). This study evaluates whether this parameterization scheme, combined with the model's unstructured mesh capability, adequately resolves Arctic vertical thermal coupling features, particularly in the Eurasian Basin. A diagnostic framework based on spatiotemporal correlation analysis is established to quantify the thermal linkage between the upper (10 m) and intermediate (AW core layer, 400 m) ocean layers. This analysis addresses two critical aspects: (1) spatiotemporal delay characteristics in vertical heat signal propagation relative to AW transport timescales, and (2) potential regime shifts in interlayer coupling mechanisms under climate warming. This diagnostic framework provides dynamic constraints for optimizing ver-

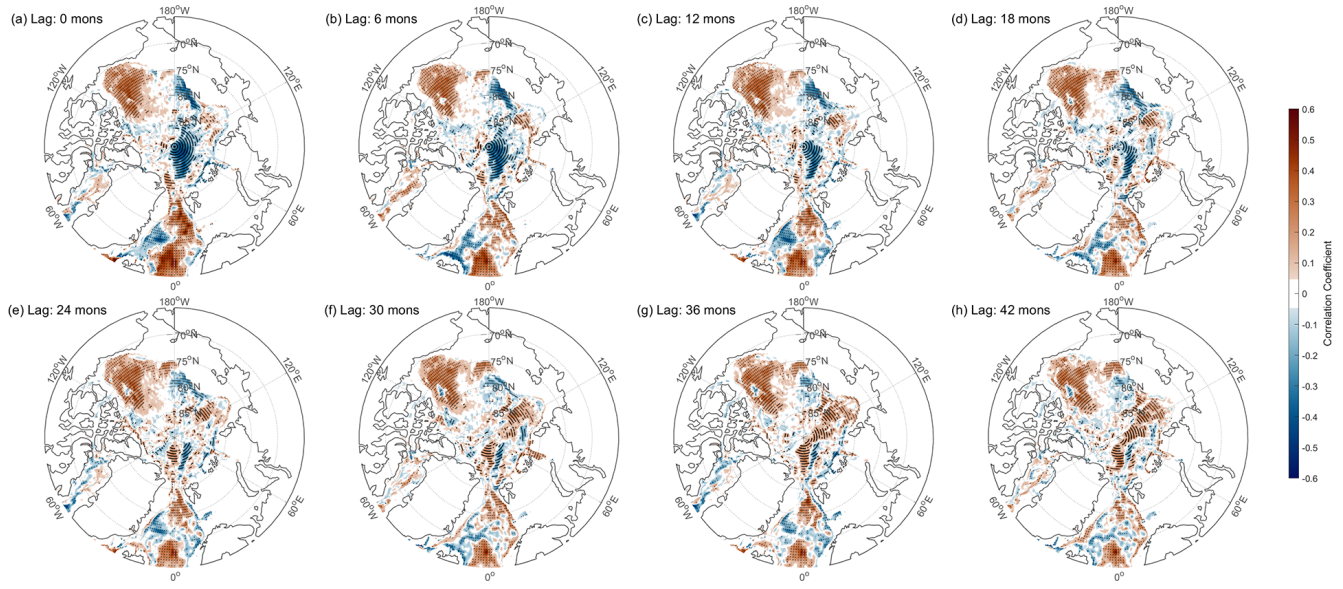

Figure 19. (a) 1960–1980 climatological mean correlation between surface (5 m) and mid-depth (400 m) temperatures. **(b–h)** Lagged correlations at 6-month intervals (lag 6 mons to 42 mons). Black dots indicate significance ($p < 0.05$).

tical mixing parameterizations while elucidating climate impacts of upper-ocean thermal variability.

During 1960–1980 baseline conditions (zero time lag), statistically significant positive correlations ($p < 0.05$) between AW layer and surface temperatures are confined to the Norwegian Sea, indicating direct advective heat modulation (Fig. 19a). Lagged correlation analysis reveals basin-scale inertial transport characteristics: localized positive correlations emerge in the Eurasian Basin at 24-month lag, expanding basin-wide by 36 months (Fig. 19b–h). This spatiotemporal inertia is attributed to: (1) basin-scale recirculation timescales required for AW mass circumpolar transport (e.g., 2-year lag between the Fram Strait and the eastern Eurasian Basin 250 m temperatures; Polyakov et al., 2020b), and (2) efficiency limitations in subsurface mixing processes.

The 1995–2020 period exhibits fundamental regime transition: immediate basin-wide positive correlations ($p < 0.05$) emerge along AW pathways (from the Fram Strait to the Eurasian Basin) under zero-lag conditions, maintaining stable correlation strength through 42-month lags (Fig. 20). This instantaneous response pattern reflects multiscale Arctic system changes: (1) increased AWCT with decreased AWCD shortens vertical diffusion pathways, indicating intensified "Atlantification" (Polyakov et al., 2017); (2) stratification weakening from sea ice loss enhances cross-layer turbulent mixing efficiency (Kwok, 2018; Onarheim et al., 2018; Polyakov et al., 2020a).

A fundamental regime shift in Arctic intermediate-to-surface thermal coupling mechanisms under climate warming is revealed through cross-temporal-scale lagged correlation diagnostics: transitioning from historical basin-scale inertial transport patterns to contemporary instantaneous response modes. This regime shift, driven by altered AW thermohaline properties and reduced stratification stability, enhances vertical heat leakage efficiency from intermediate layers. Model evaluation demonstrates that while the KPP scheme captures accelerated heat transport trends, systematic biases persist in nonlinear responses to shear mixing (Figs. 19 and 20). Future research directions emphasize developing scale-aware parameterizations incorporating high-resolution turbulence observations to improve model capabilities in predicting Arctic energy transport regime shifts.

5 Discussion

5.1 Comparison with OMIP2 models under diverse grid configurations and resolutions

To evaluate the performance of different ocean–sea ice coupled models in simulating the three-dimensional themohaline structure, particularly that of the intermediate AW layer, we further discuss five resolution-matched model pairs from OMIP2 (Wang et al., 2024). Thermohaline profile characteristics in the Eurasian and Amerasian Basins are systematically compared between high/low-resolution model pairs (solid/dashed lines), E3SMv2-MPAS, and WOA23 data (Locarnini et al., 2024; Reagan et al., 2024) to elucidate ocean model grid configuration impacts (Fig. 21).

Low-resolution models exhibit systematic biases as follows: (1) substantial underestimation of AWCT (e.g., $< 0\,^{\circ}C$ in CMCC-NEMO_51 km and FSU-HYCOM_32 km), and (2) an inability to reproduce the characteristic vertical thermohaline structure, wherein temperatures decline with depth

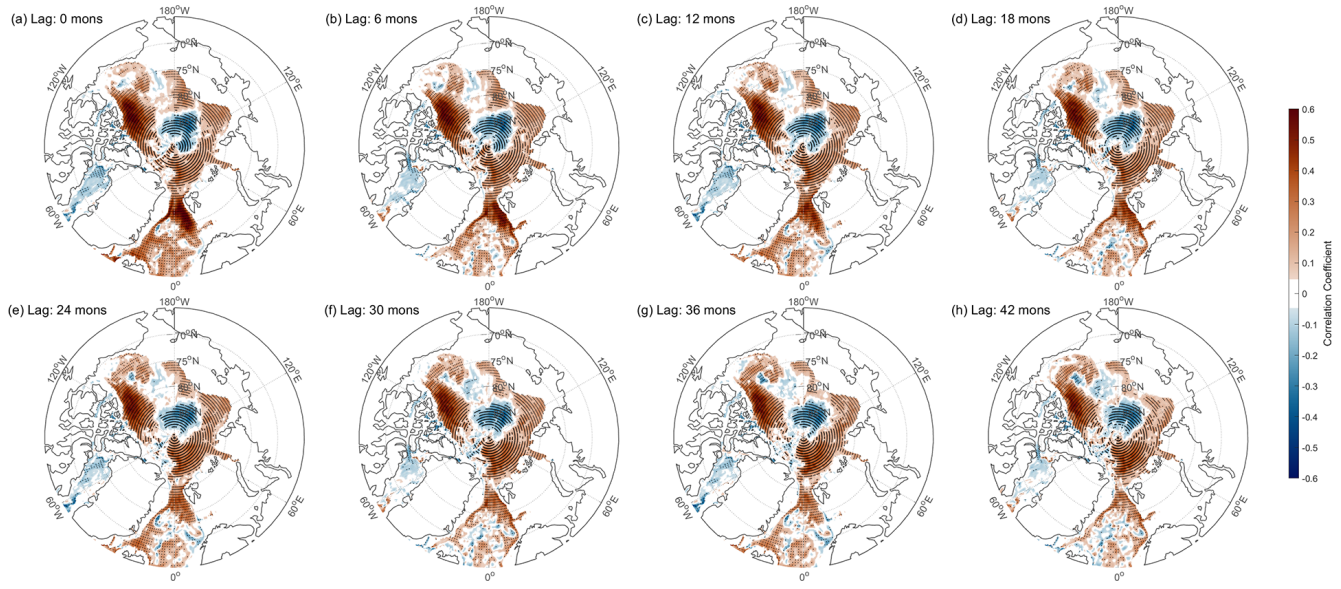

Figure 20. The same as Fig. 19, but for 1995–2020 period.

after AWCD. These challenges are particularly pronounced in the Eurasian Basin influenced by the Fram Strait branch (one of two primary AW inflow pathways) compared to the Amerasian Basin. In contrast, their high-resolution counterparts (excluding IAP-LICOM-6.8 km) demonstrate improved AWCT and vertical structure simulations. High-resolution models successfully reproduce observed zonal gradients showing AWCT decreasing from the Eurasian Basin (1.3 °C at 250 m) to the Amerasian Basin (0.7 °C at 400 m), confirming resolution enhancement benefits for oceanic frontal processes.

In the Eurasian Basin where simulation biases are most pronounced, the majority of high-resolution models – with the exception of E3SMv2-MPAS (10 km) and FESOM variants (4.5/24 km) – continue to exhibit overestimated AW layer thickness (between 0 °C isotherms). WOA23 observations indicate temperature decline to 0 °C at 800 m depth, whereas most models (e.g., CMCC-NEMO_3.2 km, FSU-HYCOM_3.6 km and IAP-LICOM_6.8 km) maintain ~ 0.5 °C at the same depth (Fig. 21a). This persistent discrepancy demonstrates that resolution enhancement alone remains insufficient to fully resolve key technical bottlenecks in Arctic Intermediate Water simulations. Notably, E3SMv2-MPAS and FESOM models exhibit strong performance.

Following the evaluation of the three-dimensional thermohaline structure simulations in the OMIP2 models, we further examine their capability to reproduce the spatial distribution of AWCT. As indicated by cross-validation within the OMIP2 framework, among the five resolution-varied model groups, only FESOM_4.5 km, MOM_3.6 km, and HYCOM_3.6 km demonstrate high AWCT spatial pattern simulation skills (Fig. 22). FESOM_4.5 km outperforms E3SMv2-MPAS (10 km) in representing the western Eurasian Basin shelf-basin gradients, but underperforms in the Amerasian Basin (Fig. 22b and c). Low-resolution models exhibit a systematic underestimation of AWCT, with FESOM_24 km being the exception, reaffirming unstructured meshes' polar ocean modeling advantages (Fig. 22h–l).

Despite comparable resolutions to other high-resolution models (e.g., ACCESS-MOM 9 km, FSU-HYCOM 32 km), unstructured mesh configurations enable refined representation of key hydrographic gateways like the Fram Strait. Compared to tripolar grid models suffering numerical dissipation near complex coastlines, variable mesh designs achieve reduced the Eurasian Basin temperature errors under equivalent computational resources. Model grid type and computational efficiency exhibit nonlinear relationships. Unstructured meshes (FESOM/MPAS) permit dynamic optimization through localized refinement in critical regions (e.g., AW intrusion pathways). This targeted refinement strategy provides new technical approaches for Arctic ocean modeling, particularly under accelerating Atlantification processes.

5.2 Sources of systematic biases and trade-offs between resolution and parameterizations

Analyses in Sect. 3 not only discussed the simulation biases of E3SMv2-MPAS but also traced their potential origins. For most biases, the primary causes can be attributed to inadequacies in physical parameterizations. First, the inadequate representation of eddy dynamics is a key source. For instance, the underestimation of freshening in the Amerasian Basin may result from the use of a fixed eddy diffusivity ($\kappa = 300\,\mathrm{m^2\,s^{-1}}$ in the Arctic), which oversmooths salinity fronts. Similarly, the model's failure to capture the seasonal variability of the AW layer likely stems from the invariant κ

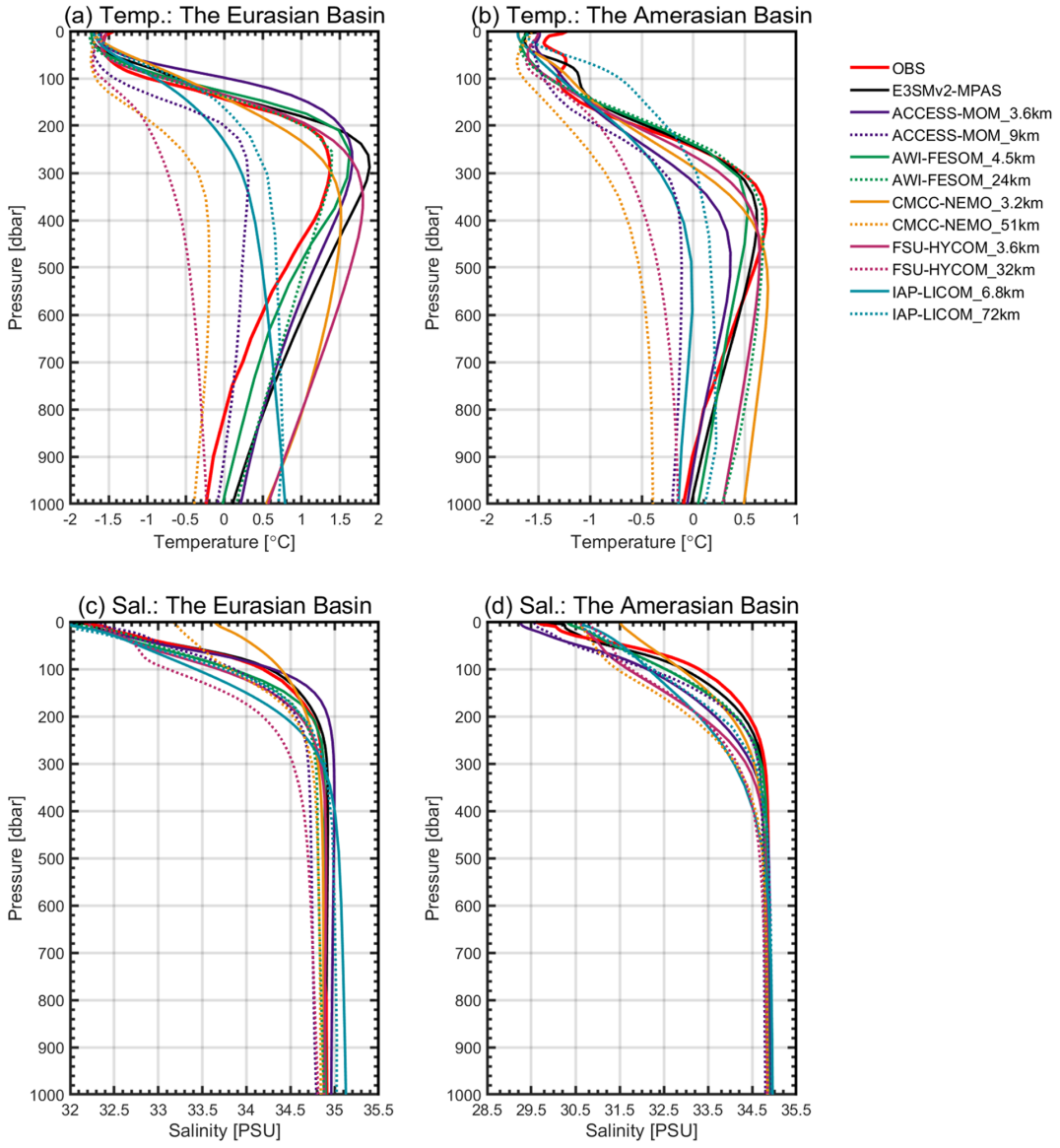

Figure 21. (a, b) 1995–2014 climatological mean temperature profiles in **(a)** the Eurasian Basin and **(b)** the Amerasian Basin: Observations (WOA23; red), E3SMv2-MPAS (black), OMIP2 models (Wang et al., 2024; dashed: low-resolution, solid: high-resolution). **(c, d)** The same as panels **(a)** and **(b)** but for salinity profiles.

in the GM scheme, which cannot respond to the seasonal cycle of sea ice retreat and associated changes in stratification. Second, limitations in vertical mixing parameterizations act as another key source. The coordinated biases in SST, SSS, and SIC in the Greenland and Barents Seas, for example, may arise from the inherent limitations of the KPP scheme's single Ri-based approach in defining turbulent states and mixing intensities within complex dynamic environments. Additionally, the misrepresentation of the warming layer in the Eurasian Basin could be linked to inappropriate background diffusion coefficients within the KPP framework.

Increasing model resolution presents an effective pathway to reduce reliance on empirical parameterizations by more directly resolving key physical processes, such as mesoscale eddies. Enhanced resolution can, to some extent, mitigate the inaccuracies of existing schemes. For instance, studies have shown that higher resolution improves the simulation of the AW layer's temperature, thickness, spatial distribution, and its decadal warming trends (Wang et al., 2024). However, the small Rossby radius of deformation (often ≤ 3 km) in the Arctic (Veneziani et al., 2022) implies that even with computationally feasible resolution increases, critical processes (e.g. mesoscale eddies, vertical mixing, and ice–ocean interactions) may remain under-resolved (Chassignet et al., 2020; Wang et al., 2018). Therefore, the development of more advanced physical parameterizations remains imperative. It is

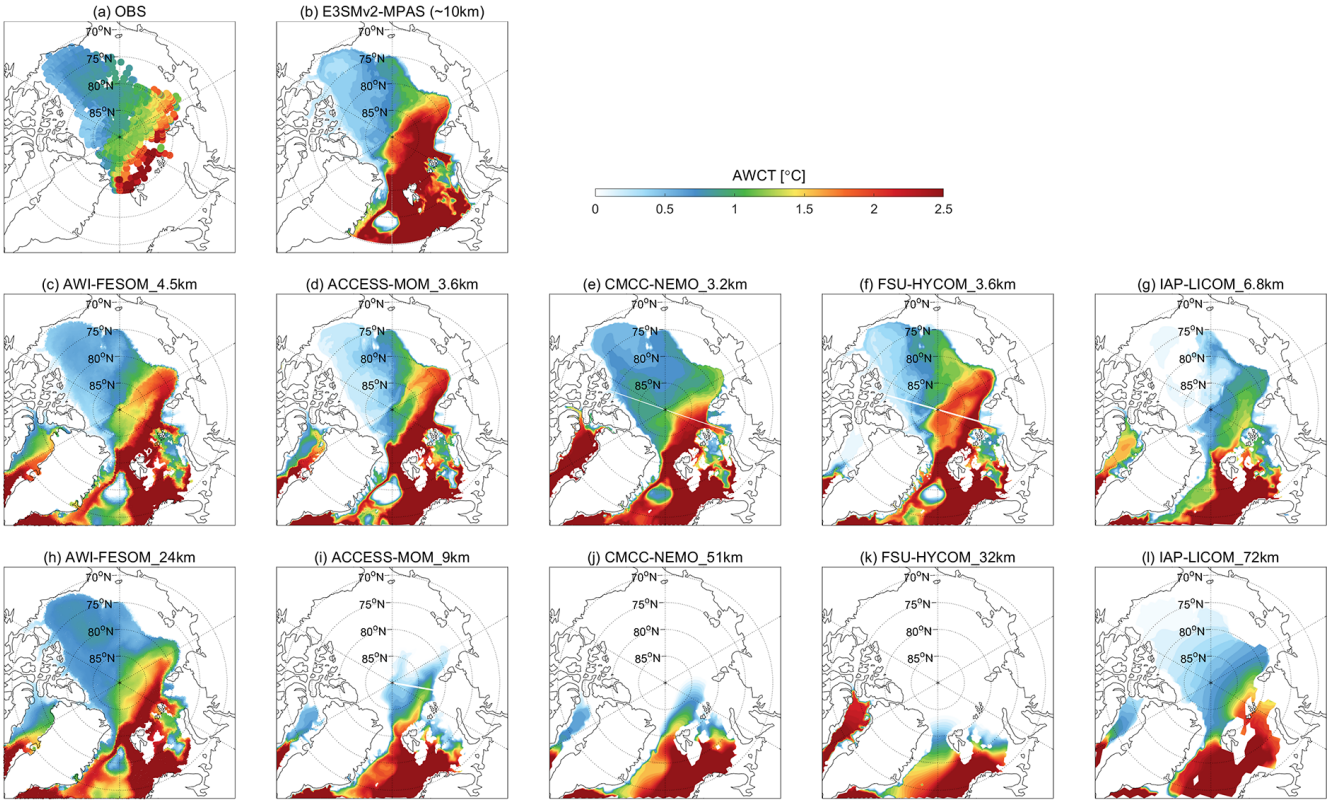

Figure 22. 1995–2018 climatological mean AWCT spatial patterns from **(a)** observations (Richards et al., 2022), **(b)** E3SMv2-MPAS, and **(c–l)** OMIP2 models (Wang et al., 2024). **(c–l)** High-resolution and corresponding low-resolution model pairs from OMIP2.

noteworthy that resolution increases have proven effective in improving the simulation of volume, heat, and freshwater transports through critical gateways such as the Fram Strait and Davis Strait (Wang et al., 2024). The Fram Strait, in particular, serves as a pivotal channel for Atlantic heat influx into the Arctic Ocean (Herbaut et al., 2022; Pnyushkov et al., 2021). In conclusion, we propose that a cost-effective strategy involves targetedly increasing resolution in key gateway regions while concurrently refining parameterizations for mesoscale eddies and vertical mixing.

5.3 Limitations of the experimental design

Due to computational resource constraints, this study adopted a two-phase simulation strategy with non-consecutive time periods: first, the model was integrated from 1958 to 1981, and the final state of this period was used as the initial condition to directly start the simulation for the 1995–2020 period. Although this approach effectively reduced computational costs, and both previous studies and our model diagnostics indicate that key upper-ocean and sea ice variables had reached a quasi-equilibrium state by 1981, skipping the continuous integration of the 1982–1994 period may introduce certain limitations. For instance, the simulation of some medium- to long-term fluctuations or memory-dependent processes might be affected. Should computational resources allow in the future, we will perform a continuous simulation from 1958 to 2020 to more accurately reproduce the evolution of the climate system.

Furthermore, since only a single JRA55 forcing cycle was applied, the deep ocean and some physical quantities may not have fully departed from the influence of the initial PHC hydrographic fields or reached complete equilibrium. This could potentially affect the stability and initial-condition independence of the simulation results. In subsequent work, given sufficient resources, we plan to carry out at least three full JRA55 forcing cycles to promote more complete adjustment of the ocean state, reduce dependence on initial conditions, and thereby enable a more comprehensive and robust evaluation of the climate performance of the E3SMv2-MPAS.

5.4 Limitations from the atmospheric forcing: the JRA55 warm bias

The JRA55 reanalysis forcing data employed in E3SMv2-MPAS exhibits a known warm bias over the central Arctic deep basin (Batrak and Müller, 2019). This bias may systematically suppress sea ice growth and induce upper-ocean warming in the simulation by enhancing downward

longwave radiation and reducing oceanic sensible heat loss. Therefore, the overestimated SST (Fig. 8c) and underestimated summer SIC (Fig. 4e–g) simulated in the central Arctic basin may be partially attributable to the inherent bias in the forcing data, rather than solely to inaccuracies in the model's physical processes.

The enhanced ice melt driven by this warm bias releases additional freshwater, leading to a stronger and shallower freshwater layer (a more pronounced halocline) in the surface ocean, which significantly strengthens the stratification stability of the upper ocean. This inhibits vertical mixing between layers and impedes the upward heat transfer from the warmer, saltier AW below. This bias may partly explain the overestimation of the intermediate AW layer temperature alongside the underestimation of the mixed-layer temperature (Fig. 12e). Future work will consider employing alternative reanalysis products or applying bias-correction methods to better constrain the impact of forcing uncertainties on simulation results.

6 Conclusions

This study systematically evaluates the Arctic ocean–sea ice simulation capabilities of E3SMv2-MPAS through multisource observations (in situ profiles, satellite remote sensing, optimum interpolation datasets) and reanalysis products (NSIDC, HadISST1, ERA5, PIOMAS, ORAS5), with focus on core parameters including sea ice (concentration/extent/thickness/volume; SIC/SIE/SIT/SIV), surface thermohaline properties (sea surface temperature/salinity; SST/SSS), three-dimensional thermohaline structures, freshwater content (FWC), gateway transports, Atlantic Water (AW) heat characteristics, and vertical thermal linkages. Spatial distribution patterns, seasonal-to-decadal variability, and three-dimensional evolutionary processes are comprehensively analyzed.

E3SMv2-MPAS demonstrates significant advantages in Arctic climatology simulations: (1) accurate representation of spatial heterogeneity in SIC, SIT, and SST (Figs. 3–5 and 8a–c); (2) realistic simulation of interannual and decadal variability in SIC, SIE, SIT, SIV and SST, along with a highly consistent reproduction of the 1995–2020 SIC decline trend compared to NSIDC observation, outperforming Hadley and ERA5 reanalysis products (Fig. 7a); (3) consistent SSS spatial patterns and seasonal evolution with leading reanalysis products including HYCOM and GLORYS12 (Fig. 9; Hall et al., 2021); (4) faithful reproduction of both the spatial distribution and long-term trend of Arctic FWC (Fig. 15); (5) accurate simulation of volume, heat, and freshwater transports through key Arctic gateways, capturing their observed magnitudes and essential variability trends (Fig. 16).

E3SMv2-MPAS demonstrates exceptional capability in simulating the three-dimensional thermohaline structure and variability of the AW layer, accurately capturing its key thermodynamic and dynamic processes in the Arctic Ocean: (1) precise reproduction of AW layer thickness/depth and core temperature (Figs. 10 and 17); (2) effective capture of AW warming trends including decadal-scale intermediate layer heating and vertical shoaling of warm cores (Figs. 11 and 13); (3) realistic simulation of accelerated Atlantification processes, evidenced by post-2000 intensification in AW core temperature and heat content while reduced AW core depth, upper boundary and layer thickness, and instantaneous surface-intermediate heat transfer in the Eurasian Basin (Figs. 18–20). Additional breakthroughs include successful representation of solar-driven seasonal upper-ocean thermal cycles (Fig. 12) and inter-basin water mass gradient evolution from the Eurasian Basin to the Amerasian Basin (e.g., AW thermohaline attenuation, vertical stratification shifts, and surface freshwater transport effects; Fig. 14). These advancements establish critical numerical platforms for investigating Arctic stratification destabilization and cross-scale energy transfer mechanisms.

Notwithstanding these achievements, key limitations persist: (1) systematic overestimation of SIT in the Canadian Basin (0.5–1 m bias; Fig. 5); (2) coordinated underestimation of SST/SSS and overestimation of SIC in the Greenland and Barent Seas (Figs. 3–4, 8a–c and 9a–c); (3) residual overestimation of AW core temperature (0–1 °C) and errors in seasonal Atlantification phase (Figs. 10 and 12); (4) asymmetries in regional decadal thermohaline evolution (e.g., underestimated upper-layer warming and overestimated deep warming in the Eurasian Basin, unresolved mid-layer warming and upper-layer freshening trends in the Amerasian Basin; Fig. 13).

This study confirms that E3SMv2-MPAS significantly enhances simulation capabilities for Arctic oceanic thermal structures and cross-layer coupling processes through high-resolution unstructured meshes, establishing crucial technical references for polar climate model development in the CMIP7 era.

Code and data availability. The E3SM model code is publicly available via the https://github.com/E3SM-Project/E3SM/releases (last access: 28 June 2023). Instructions on how to configure and execute E3SM are available at https://e3sm.org/model/running-e3sm/e3sm-quick-start/ (last access: 15 March 2025). All simulations detailed in Sect. 2.1 can be regenerated by executing the code hosted in this repository: https://doi.org/10.5281/zenodo.15493256 (Lv, 2025). Preprocessing of E3SMv2-MPAS outputs utilized nco-5.1.1, accessible through the https://nco.sourceforge.net/ (last access: 16 June 2025). The JRA55-v1.5 atmospheric forcing data driving the simulations were obtained from the https://aims2.llnl.gov/search/input4mips/ (last access: 10 March 2025). ETOPO 2022 bathymetry was derived from the https://www.ncei.noaa.gov/products/etopo-global-relief-model (last access: 10 May 2025). Model evaluations employed the following observational and reanalysis products: Sea ice concentration: NSIDC (https://noaadata.apps.nsidc.org/NOAA/G02202_V4/

north/aggregate/, last access: 5 June 2025), Met Office Hadley Centre observational datasets (https://www.metoffice.gov.uk/hadobs/, last access: 5 June 2025), and ERA5 monthly single-level data (https://cds.climate.copernicus.eu/datasets/reanalysis-era5-single-levels-monthly-means?tab=overview, last access: 5 June 2025); Sea ice extent: NSIDC (https://doi.org/10.7265/N5K072F8, Fetterer et al., 2017); Sea ice thickness and sea ice volume: PIOMAS (http://psc.apl.uw.edu/research/projects/arctic-sea-ice-volume-anomaly/data/model_gri, last access: 5 June 2025), PIOMAS-20C reconstruction (https://psc.apl.uw.edu/research/projects/piomas-20c/, last access: 15 June 2025) and CS2SMOS gridded products (https://data.meereisportal.de/data/cs2smos_awi/v206/n, last access: 23 August 2025); Sea surface properties: OISST (https://www.ncei.noaa.gov/products/optimum-interpolation-sst, last access: 21 January 2025) and OISSS (https://www.esr.org/data-products/oisss/overview/, last access: 21 January 2025); Oceanographic profiles: WOA2023 (https://www.ncei.noaa.gov/products/world-ocean-atlas, last access: 24 February 2025), EN.4.2.2 objective analyses (https://www.metoffice.gov.uk/hadobs/en4/, last access: 2 June 2024); Sea surface height: ORAS5 (https://cds.climate.copernicus.eu/datasets/reanalysis-oras5?tab=overview, last access: 23 February 2025); Ocean heat content: IAP (http://www.ocean.iap.ac.cn/ftp/cheng/IAPv4.2_Ocean_heat_content_0_6000m/, last access: 24 August 2025); Surface albedo: CLARA-A3 (https://doi.org/10.5676/EUM_SAF_CM/CLARA_AVHRR/V003, Karlsson et al., 2023). In situ observational profiles from four key Arctic regions (the western/eastern Eurasian Basin, the Chukchi Sea, and the Beaufort Sea), thermohaline profiles and Atlantic Water core temperature outputs from five OMIP2 ensemble groups, and Atlantic Water core temperature and depth observational benchmarks, are described in the main text. Detailed metadata specifications and data access instructions for these datasets are provided in the corresponding references cited therein.

Supplement. The supplement related to this article is available online at https://doi.org/10.5194/gmd-18-8535-2025-supplement.

Author contributions. XL led the manuscript writing and paper analysis. XL, YC, and HD performed the installation, configuration, and execution of the E3SMv2-MPAS model. HW, KR, and YW were primarily responsible for the conceptualization of the study and manuscript revisions. All co-authors reviewed and commented on the final version of the manuscript.

Competing interests. The contact author has declared that none of the authors has any competing interests.

Disclaimer. Publisher's note: Copernicus Publications remains neutral with regard to jurisdictional claims made in the text, published maps, institutional affiliations, or any other geographical representation in this paper. While Copernicus Publications makes every effort to include appropriate place names, the final responsibility lies with the authors. Views expressed in the text are those of the authors and do not necessarily reflect the views of the publisher.

Acknowledgements. The public availability of different observational data sets and reanalysis data used in this work is a great help for model development, so the efforts of respective working groups are appreciated.

Financial support. This research has been supported by the National Key Research and Development Program of China (grant no. 2021YFC3101503), the Department of Science and Technology of Hunan Province (grant nos. 2022RC3070 and 2023JJ10053), the Science and Technology Innovation Program of Hunan Province (grant no. 2022RC3070), and the Hunan Provincial Natural Science Foundation of China (grant no. 2023JJ10053)

Review statement. This paper was edited by Cynthia Whaley and reviewed by Xi Liang and one anonymous referee.

References

Aagaard, K. and Carmack, E. C.: The role of sea ice and other fresh water in the Arctic circulation, J. Geophys. Res., 94, 14485–14498, https://doi.org/10.1029/JC094iC10p14485, 1989.

Aagaard, K., Coachman, L. K., and Carmack, E.: On the halocline of the Arctic Ocean, Deep-Sea Res. Pt. A, 28, 529–545, https://doi.org/10.1016/0198-0149(81)90115-1, 1981.

Aksenov, Y., Karcher, M., Proshutinsky, A., Gerdes, R., De Cuevas, B., Golubeva, E., Kauker, F., Nguyen, A. T., Platov, G. A., Wadley, M., Watanabe, E., Coward, A. C., and Nurser, A. J. G.: Arctic pathways of Pacific Water: Arctic Ocean Model Intercomparison experiments, J. Geophys. Res.-Oceans, 121, 27–59, https://doi.org/10.1002/2015JC011299, 2016.

Årthun, M., Eldevik, T., Smedsrud, L. H., Skagseth, Ø., and Ingvaldsen, R. B.: Quantifying the Influence of Atlantic Heat on Barents Sea Ice Variability and Retreat, J. Climate, 25, 4736–4743, https://doi.org/10.1175/JCLI-D-11-00466.1, 2012.

Årthun, M., Eldevik, T., and Smedsrud, L. H.: The Role of Atlantic Heat Transport in Future Arctic Winter Sea Ice Loss, J. Climate, 32, 3327–3341, https://doi.org/10.1175/JCLI-D-18-0750.1, 2019.

Arzel, O., Fichefet, T., Goosse, H., and Dufresne, J.-L.: Causes and impacts of changes in the Arctic freshwater budget during the twentieth and twenty-first centuries in an AOGCM, Clim. Dynam., 30, 37–58, https://doi.org/10.1007/s00382-007-0258-5, 2007.

Barton, B. I., Lenn, Y.-D., and Lique, C.: Observed Atlantification of the Barents Sea Causes the Polar Front to Limit the Expansion of Winter Sea Ice, J. Phys. Oceanogr., 48, 1849–1866, https://doi.org/10.1175/JPO-D-18-0003.1, 2018.

Batrak, Y. and Müller, M.: On the warm bias in atmospheric reanalyses induced by the missing snow over Arctic sea-ice, Nat. Commun., 10, 4170, https://doi.org/10.1038/s41467-019-11975-3, 2019.

Calvin, K., Dasgupta, D., Krinner, G., Mukherji, A., Thorne, P. W., Trisos, C., Romero, J., Aldunce, P., Barrett, K., Blanco, G., Cheung, W. W. L., Connors, S., Denton, F., Diongue-Niang, A., Dodman, D., Garschagen, M., Geden, O., Hayward, B., Jones, C., Jotzo, F., Krug, T., Lasco, R., Lee, Y.-Y., Masson-Delmotte, V., Meinshausen, M., Mintenbeck, K., Mokssit, A., Otto, F. E. L., Pathak, M., Pirani, A., Poloczanska, E., Pörtner, H.-O., Revi, A., Roberts, D. C., Roy, J., Ruane, A. C., Skea, J., Shukla, P. R., Slade, R., Slangen, A., Sokona, Y., Sörensson, A. A., Tignor, M., Van Vuuren, D., Wei, Y.-M., Winkler, H., Zhai, P., Zommers, Z., Hourcade, J.-C., Johnson, F. X., Pachauri, S., Simpson, N. P., Singh, C., Thomas, A., Totin, E., Arias, P., Bustamante, M., Elgizouli, I., Flato, G., Howden, M., Méndez-Vallejo, C., Pereira, J. J., Pichs-Madruga, R., Rose, S. K., Saheb, Y., Sánchez Rodríguez, R., Ürge-Vorsatz, D., Xiao, C., Yassaa, N., Alegría, A., Armour, K., Bednar-Friedl, B., Blok, K., Cissé, G., Dentener, F., Eriksen, S., Fischer, E., Garner, G., Guivarch, C., Haasnoot, M., Hansen, G., Hauser, M., Hawkins, E., Hermans, T., Kopp, R., Leprince-Ringuet, N., Lewis, J., Ley, D., Ludden, C., Niamir, L., Nicholls, Z., Some, S., Szopa, S., Trewin, B., Van Der Wijst, K.-I., Winter, G., Witting, M., Birt, A., and Ha, M.: IPCC, 2023: Climate Change 2023: Synthesis Report, in: Contribution of Working Groups I, II and III to the Sixth Assessment Report of the Intergovernmental Panel on Climate Change, edited by: Core Writing Team, Lee, H., and Romero, J., IPCC – Intergovernmental Panel on Climate Change, Geneva, Switzerland, https://doi.org/10.59327/IPCC/AR6-9789291691647, 2023.

Carmack, E., Polyakov, I., Padman, L., Fer, I., Hunke, E., Hutchings, J., Jackson, J., Kelley, D., Kwok, R., Layton, C., Melling, H., Perovich, D., Persson, O., Ruddick, B., Timmermans, M.-L., Toole, J., Ross, T., Vavrus, S., and Winsor, P.: Toward Quantifying the Increasing Role of Oceanic Heat in Sea Ice Loss in the New Arctic, B. Am. Meteorol. Soc., 96, 2079–2105, https://doi.org/10.1175/BAMS-D-13-00177.1, 2015.

Chassignet, E. P., Yeager, S. G., Fox-Kemper, B., Bozec, A., Castruccio, F., Danabasoglu, G., Horvat, C., Kim, W. M., Koldunov, N., Li, Y., Lin, P., Liu, H., Sein, D. V., Sidorenko, D., Wang, Q., and Xu, X.: Impact of horizontal resolution on global ocean–sea ice model simulations based on the experimental protocols of the Ocean Model Intercomparison Project phase 2 (OMIP-2), Geosci. Model Dev., 13, 4595–4637, https://doi.org/10.5194/gmd-13-4595-2020, 2020.

Chen, C., Gao, G., Zhang, Y., Beardsley, R. C., Lai, Z., Qi, J., and Lin, H.: Circulation in the Arctic Ocean: Results from a high-resolution coupled ice-sea nested Global-FVCOM and Arctic-FVCOM system, Prog. Oceanogr., 141, 60–80, https://doi.org/10.1016/j.pocean.2015.12.002, 2016.

Cheng, L., Trenberth, K. E., Fasullo, J., Boyer, T., Abraham, J., and Zhu, J.: Improved estimates of ocean heat content from 1960 to 2015, Sci. Adv., 3, e1601545, https://doi.org/10.1126/sciadv.1601545, 2017.

Cheng, L., Trenberth, K. E., Gruber, N., Abraham, J. P., Fasullo, J. T., Li, G., Mann, M. E., Zhao, X., and Zhu, J.: Improved Estimates of Changes in Upper Ocean Salinity and the Hydrological Cycle, J. Climate, 33, 10357–10381, https://doi.org/10.1175/JCLI-D-20-0366.1, 2020.

Cheng, L., Pan, Y., Tan, Z., Zheng, H., Zhu, Y., Wei, W., Du, J., Yuan, H., Li, G., Ye, H., Gouretski, V., Li, Y., Trenberth, K. E., Abraham, J., Jin, Y., Reseghetti, F., Lin, X., Zhang, B., Chen, G., Mann, M. E., and Zhu, J.: IAPv4 ocean temperature and ocean heat content gridded dataset, Earth Syst. Sci. Data, 16, 3517–3546, https://doi.org/10.5194/essd-16-3517-2024, 2024.

Curry, B., Lee, C. M., Petrie, B., Moritz, R. E., and Kwok, R.: Multiyear Volume, Liquid Freshwater, and Sea Ice Transports through Davis Strait, 2004–10, J. Phys. Oceanogr., 44, 1244–1266, https://doi.org/10.1175/JPO-D-13-0177.1, 2014.

Danilov, S., Sidorenko, D., Wang, Q., and Jung, T.: The Finite-volumE Sea ice–Ocean Model (FESOM2), Geosci. Model Dev., 10, 765–789, https://doi.org/10.5194/gmd-10-765-2017, 2017.

D'Asaro, E. A.: The Energy Flux from the Wind to Near-Inertial Motions in the Surface Mixed Layer, J. Phys. Oceanogr., 15, 1043–1059, https://doi.org/10.1175/1520-0485(1985)015<1043:TEFFTW>2.0.CO;2, 1985.

Davis, P. E. D., Lique, C., Johnson, H. L., and Guthrie, J. D.: Competing Effects of Elevated Vertical Mixing and Increased Freshwater Input on the Stratification and Sea Ice Cover in a Changing Arctic Ocean, J. Phys. Oceanogr., 46, 1531–1553, https://doi.org/10.1175/JPO-D-15-0174.1, 2016.

Docquier, D. and Koenigk, T.: A review of interactions between ocean heat transport and Arctic sea ice, Environ. Res. Lett., 16, 123002, https://doi.org/10.1088/1748-9326/ac30be, 2021.

Dörr, J., Årthun, M., Eldevik, T., and Madonna, E.: Mechanisms of Regional Winter Sea-Ice Variability in a Warming Arctic, J. Climate, 34, 8635–8653, https://doi.org/10.1175/JCLI-D-21-0149.1, 2021.

Fetterer, F., Knowles, K., Meier, W. N., Savoie, M., and Windnagel, A. K.: Sea Ice Index, Version 3, NSIDC [data set], https://doi.org/10.7265/N5K072F8, 2017.

Fu, C., Pennelly, C., Garcia-Quintana, Y., and Myers, P. G.: Pulses of Cold Atlantic Water in the Arctic Ocean From an Ocean Model Simulation, J. Geophys. Res.-Oceans, 128, e2023JC019663, https://doi.org/10.1029/2023JC019663, 2023.

Gent, P. R. and Mcwilliams, J. C.: Isopycnal Mixing in Ocean Circulation Models, J. Phys. Oceanogr., 20, 150–155, https://doi.org/10.1175/1520-0485(1990)020<0150:IMIOCM>2.0.CO;2, 1990.

Golaz, J., Caldwell, P. M., Van Roekel, L. P., Petersen, M. R., Tang, Q., Wolfe, J. D., Abeshu, G., Anantharaj, V., Asay-Davis, X. S., Bader, D. C., Baldwin, S. A., Bisht, G., Bogenschutz, P. A., Branstetter, M., Brunke, M. A., Brus, S. R., Burrows, S. M., Cameron-Smith, P. J., Donahue, A. S., Deakin, M., Easter, R. C., Evans, K. J., Feng, Y., Flanner, M., Foucar, J. G., Fyke, J. G., Griffin, B. M., Hannay, C., Harrop, B. E., Hoffman, M. J., Hunke, E. C., Jacob, R. L., Jacobsen, D. W., Jeffery, N., Jones, P. W., Keen, N. D., Klein, S. A., Larson, V. E., Leung, L. R., Li, H., Lin, W., Lipscomb, W. H., Ma, P., Mahajan, S., Maltrud, M. E., Mametjanov, A., McClean, J. L., McCoy, R. B., Neale, R. B., Price, S. F., Qian, Y., Rasch, P. J., Reeves Eyre, J. E. J., Riley, W. J., Ringler, T. D., Roberts, A. F., Roesler, E. L., Salinger, A. G., Shaheen, Z., Shi, X., Singh, B., Tang, J., Taylor, M. A., Thornton, P. E., Turner, A. K., Veneziani, M., Wan, H., Wang, H., Wang, S., Williams, D. N., Wolfram, P. J., Worley, P. H., Xie, S., Yang, Y., Yoon, J., Zelinka, M. D., Zender, C. S., Zeng, X.,

Zhang, C., Zhang, K., Zhang, Y., Zheng, X., Zhou, T., and Zhu, Q.: The DOE E3SM Coupled Model Version 1: Overview and Evaluation at Standard Resolution, J. Adv. Model. Earth Syst., 11, 2089–2129, https://doi.org/10.1029/2018MS001603, 2019.

Golaz, J., Van Roekel, L. P., Zheng, X., Roberts, A. F., Wolfe, J. D., Lin, W., Bradley, A. M., Tang, Q., Maltrud, M. E., Forsyth, R. M., Zhang, C., Zhou, T., Zhang, K., Zender, C. S., Wu, M., Wang, H., Turner, A. K., Singh, B., Richter, J. H., Qin, Y., Petersen, M. R., Mametjanov, A., Ma, P., Larson, V. E., Krishna, J., Keen, N. D., Jeffery, N., Hunke, E. C., Hannah, W. M., Guba, O., Griffin, B. M., Feng, Y., Engwirda, D., Di Vittorio, A. V., Dang, C., Conlon, L. M., Chen, C., Brunke, M. A., Bisht, G., Benedict, J. J., Asay-Davis, X. S., Zhang, Y., Zhang, M., Zeng, X., Xie, S., Wolfram, P. J., Vo, T., Veneziani, M., Tesfa, T. K., Sreepathi, S., Salinger, A. G., Reeves Eyre, J. E. J., Prather, M. J., Mahajan, S., Li, Q., Jones, P. W., Jacob, R. L., Huebler, G. W., Huang, X., Hillman, B. R., Harrop, B. E., Foucar, J. G., Fang, Y., Comeau, D. S., Caldwell, P. M., Bartoletti, T., Balaguru, K., Taylor, M. A., McCoy, R. B., Leung, L. R., and Bader, D. C.: The DOE E3SM Model Version 2: Overview of the Physical Model and Initial Model Evaluation, J. Adv. Model. Earth Syst., 14, e2022MS003156, https://doi.org/10.1029/2022MS003156, 2022.

Good, S. A., Martin, M. J., and Rayner, N. A.: EN4: Quality controlled ocean temperature and salinity profiles and monthly objective analyses with uncertainty estimates, J. Geophys. Res.-Oceans, 118, 6704–6716, https://doi.org/10.1002/2013JC009067, 2013.

Haine, T. W. N., Curry, B., Gerdes, R., Hansen, E., Karcher, M., Lee, C., Rudels, B., Spreen, G., De Steur, L., Stewart, K. D., and Woodgate, R.: Arctic freshwater export: Status, mechanisms, and prospects, Global Planet. Change, 125, 13–35, https://doi.org/10.1016/j.gloplacha.2014.11.013, 2015.

Haine, T. W. N., Siddiqui, A. H., and Jiang, W.: Arctic freshwater impact on the Atlantic Meridional Overturning Circulation: status and prospects, Philos. T. Roy. Soc. A, 381, 20220185, https://doi.org/10.1098/rsta.2022.0185, 2023.

Hall, S. B., Subrahmanyam, B., and Morison, J. H.: Intercomparison of Salinity Products in the Beaufort Gyre and Arctic Ocean, Remote Sens., 14, 71, https://doi.org/10.3390/rs14010071, 2021.

Heidinger, A. K., Straka, W. C., Molling, C. C., Sullivan, J. T., and Wu, X.: Deriving an inter-sensor consistent calibration for the AVHRR solar reflectance data record, Int. J. Remote Sens., 31, 6493–6517, https://doi.org/10.1080/01431161.2010.496472, 2010.

Herbaut, C., Houssais, M., Blaizot, A., and Molines, J.: A Role for the Ocean in the Winter Sea Ice Distribution North of Svalbard, J. Geophys. Res.-Oceans, 127, e2021JC017852, https://doi.org/10.1029/2021JC017852, 2022.

Hersbach, H., Bell, B., Berrisford, P., Hirahara, S., Horányi, A., Muñoz-Sabater, J., Nicolas, J., Peubey, C., Radu, R., Schepers, D., Simmons, A., Soci, C., Abdalla, S., Abellan, X., Balsamo, G., Bechtold, P., Biavati, G., Bidlot, J., Bonavita, M., Chiara, G., Dahlgren, P., Dee, D., Diamantakis, M., Dragani, R., Flemming, J., Forbes, R., Fuentes, M., Geer, A., Haimberger, L., Healy, S., Hogan, R. J., Hólm, E., Janisková, M., Keeley, S., Laloyaux, P., Lopez, P., Lupu, C., Radnoti, G., Rosnay, P., Rozum, I., Vamborg, F., Villaume, S., and Thépaut, J.: The ERA5 global reanalysis, Q. J. Roy. Meteorol. Soc., 146, 1999–2049, https://doi.org/10.1002/qj.3803, 2020.

Heuzé, C., Zanowski, H., Karam, S., and Muilwijk, M.: The Deep Arctic Ocean and Fram Strait in CMIP6 Models, J. Climate, 36, 2551–2584, https://doi.org/10.1175/JCLI-D-22-0194.1, 2023.

Hinrichs, C., Wang, Q., Koldunov, N., Mu, L., Semmler, T., Sidorenko, D., and Jung, T.: Atmospheric Wind Biases: A Challenge for Simulating the Arctic Ocean in Coupled Models?, J. Gephys. Res.-Oceans, 126, e2021JC017565, https://doi.org/10.1029/2021JC017565, 2021.

Hoch, K. E., Petersen, M. R., Brus, S. R., Engwirda, D., Roberts, A. F., Rosa, K. L., and Wolfram, P. J.: MPAS-Ocean Simulation Quality for Variable-Resolution North American Coastal Meshes, J. Adv. Model. Earth Syst., 12, e2019MS001848, https://doi.org/10.1029/2019MS001848, 2020.

Holloway, G., Dupont, F., Golubeva, E., Häkkinen, S., Hunke, E., Jin, M., Karcher, M., Kauker, F., Maltrud, M., Morales Maqueda, M. A., Maslowski, W., Platov, G., Stark, D., Steele, M., Suzuki, T., Wang, J., and Zhang, J.: Water properties and circulation in Arctic Ocean models, J. Geophys. Res., 112, 2006JC003642, https://doi.org/10.1029/2006JC003642, 2007.

Huang, B., Liu, C., Banzon, V., Freeman, E., Graham, G., Hankins, B., Smith, T., and Zhang, H.-M.: Improvements of the Daily Optimum Interpolation Sea Surface Temperature (DOISST) Version 2.1, J. Climate, 34, 2923–2939, https://doi.org/10.1175/JCLI-D-20-0166.1, 2021.

Huo, Y., Wang, H., Veneziani, M., Comeau, D., Osinski, R., Hillman, B. R., Roesler, E. L., Maslowski, W., Rasch, P. J., Weijer, W., Baxter, I., Fu, Q., Garuba, O. A., Ma, W., Seefeldt, M. W., Sweeney, A. J., Wu, M., Zhang, J., Zhang, X., Zhang, Y., Asay-Davis, X. S., Craig, A., Lee, Y. J., and Zhang, S.: E3SM-Arctic: Regionally Refined Coupled Model for Advanced Understanding of Arctic Systems Interactions, J. Adv. Model. Earth Syst., 17, e2024MS004726, https://doi.org/10.1029/2024MS004726, 2025.

Ilıcak, M., Drange, H., Wang, Q., Gerdes, R., Aksenov, Y., Bailey, D., Bentsen, M., Biastoch, A., Bozec, A., Böning, C., Cassou, C., Chassignet, E., Coward, A. C., Curry, B., Danabasoglu, G., Danilov, S., Fernandez, E., Fogli, P. G., Fujii, Y., Griffies, S. M., Iovino, D., Jahn, A., Jung, T., Large, W. G., Lee, C., Lique, C., Lu, J., Masina, S., George Nurser, A. J., Roth, C., Salas Y Mélia, D., Samuels, B. L., Spence, P., Tsujino, H., Valcke, S., Voldoire, A., Wang, X., and Yeager, S. G.: An assessment of the Arctic Ocean in a suite of interannual CORE-II simulations. Part III: Hydrography and fluxes, Ocean Model., 100, 141–161, https://doi.org/10.1016/j.ocemod.2016.02.004, 2016.

Karami, M. P., Myers, P. G., De Vernal, A., Tremblay, L. B., and Hu, X.: The role of Arctic gateways on sea ice and circulation in the Arctic and North Atlantic Oceans: a sensitivity study with an ocean–sea-ice model, Clim. Dynam., 57, 2129–2151, https://doi.org/10.1007/s00382-021-05798-6, 2021.

Karlsson, K.-G., Riihelä, A., Trentmann, J., Stengel, M., Solodovnik, I., Meirink, J. F., Devasthale, A., Jääskeläinen, E., Kallio-Myers, V., Eliasson, S., Benas, N., Johansson, E., Stein, D., Finkensieper, S., Håkansson, N., Akkermans, T., Clerbaux, N., Selbach, N., Marc, S., and Hollmann, R.: CLARA-A3: CM SAF cLoud, Albedo and surface RAdiation dataset from AVHRR data – Edition 3 (3.0), Satellite Application Facility on Climate Monitoring [data set], https://doi.org/10.5676/EUM_SAF_CM/CLARA_AVHRR/V003, 2023.

Karpouzoglou, T., De Steur, L., Smedsrud, L. H., and Sumata, H.: Observed Changes in the Arctic Freshwater Outflow in Fram Strait, J. Geophys. Res.-Oceans, 127, e2021JC018122, https://doi.org/10.1029/2021JC018122, 2022.

Kelly, S. J., Proshutinsky, A., Popova, E. K., Aksenov, Y. K., and Yool, A.: On the Origin of Water Masses in the Beaufort Gyre, J. Geophys. Res.-Oceans, 124, 4696–4709, https://doi.org/10.1029/2019JC015022, 2019.

Khosravi, N., Wang, Q., Koldunov, N., Hinrichs, C., Semmler, T., Danilov, S., and Jung, T.: The Arctic Ocean in CMIP6 Models: Biases and Projected Changes in Temperature and Salinity, Earth's Future, 10, e2021EF002282, https://doi.org/10.1029/2021EF002282, 2022.

Kwok, R.: Arctic sea ice thickness, volume, and multiyear ice coverage: losses and coupled variability (1958–2018), Environ. Res. Lett., 13, 105005, https://doi.org/10.1088/1748-9326/aae3ec, 2018.

Landrum, L. and Holland, M. M.: Extremes become routine in an emerging new Arctic, Nat. Clim. Change, 10, 1108–1115, https://doi.org/10.1038/s41558-020-0892-z, 2020.

Large, W. G., McWilliams, J. C., and Doney, S. C.: Oceanic vertical mixing: A review and a model with a nonlocal boundary layer parameterization, Rev. Geophys., 32, 363–403, https://doi.org/10.1029/94RG01872, 1994.

Laxon, S. W., Giles, K. A., Ridout, A. L., Wingham, D. J., Willatt, R., Cullen, R., Kwok, R., Schweiger, A., Zhang, J., Haas, C., Hendricks, S., Krishfield, R., Kurtz, N., Farrell, S., and Davidson, M.: CryoSat-2 estimates of Arctic sea ice thickness and volume, Geophys. Res. Lett., 40, 732–737, https://doi.org/10.1002/grl.50193, 2013.

Liang, X. and Losch, M.: On the Effects of Increased Vertical Mixing on the Arctic Ocean and Sea Ice, J. Geophys. Res.-Oceans, 123, 9266–9282, https://doi.org/10.1029/2018JC014303, 2018.

Lind, S., Ingvaldsen, R. B., and Furevik, T.: Arctic warming hotspot in the northern Barents Sea linked to declining sea-ice import, Nat. Clim. Change, 8, 634–639, https://doi.org/10.1038/s41558-018-0205-y, 2018.

Lipscomb, W. H. and Ringler, T. D.: An Incremental Remapping Transport Scheme on a Spherical Geodesic Grid, Mon. Weather Rev., 133, 2335–2350, https://doi.org/10.1175/MWR2983.1, 2005.

Liu, W., Liu, Y., and Zhao, S.: Global mode simulation results comparison between icosahedron spherical mesh and latitude-longitude mesh in China, J. Nanjing Univers. Inf. Sci. Technol., 8, 146–151, https://doi.org/10.13878/j.cnki.jnuist.2016.02.006, 2016.

Locarnini, R. A., Mishonov, A. V., Baranova, O. K., Reagan, J. R., Boyer, T. P., Seidov, D., Wang, Z., Garcia, H. E., Bouchard, C., Cross, S. L., Paver, C. R., and Dukhovskoy, D.: World Ocean Atlas 2023, Volume 1: Temperature, NOAA, https://doi.org/10.25923/54BH-1613, 2024.

Long, Z., Perrie, W., Zhang, M., and Liu, Y.: Responses of Atlantic Water Inflow Through Fram Strait to Arctic Storms, Geophys. Res. Lett., 51, e2023GL107777, https://doi.org/10.1029/2023GL107777, 2024.

Lv, X.: E3SMv2-MPAS, Zenodo [data set], https://doi.org/10.5281/zenodo.15493256, 2025.

Meier, W., Fetterer, F., Windnagel, A., and Stewart, S.: NOAA/NSIDC Climate Data Record of Passive Microwave Sea Ice Concentration, Version 4, National Snow and Ice Data Center [data set], https://doi.org/10.7265/EFMZ-2T65, 2021.

Melnichenko, O., Hacker, P., Maximenko, N., Lagerloef, G., and Potemra, J.: Optimum interpolation analysis of Aquarius sea surface salinity, J. Geophys. Res.-Oceans, 121, 602–616, https://doi.org/10.1002/2015JC011343, 2016.

Meyer, A., Fer, I., Sundfjord, A., and Peterson, A. K.: Mixing rates and vertical heat fluxes north of Svalbard from Arctic winter to spring, J. Geophys. Res.-Oceans, 122, 4569–4586, https://doi.org/10.1002/2016JC012441, 2017.

Muilwijk, M., Nummelin, A., Heuzé, C., Polyakov, I. V., Zanowski, H., and Smedsrud, L. H.: Divergence in Climate Model Projections of Future Arctic Atlantification, J. Climate, 36, 1727–1748, https://doi.org/10.1175/JCLI-D-22-0349.1, 2023.

Onarheim, I. H., Eldevik, T., Smedsrud, L. H., and Stroeve, J. C.: Seasonal and Regional Manifestation of Arctic Sea Ice Loss, J. Climate, 31, 4917–4932, https://doi.org/10.1175/JCLI-D-17-0427.1, 2018.

Pan, R., Shu, Q., Wang, Q., Wang, S., Song, Z., He, Y., and Qiao, F.: Future Arctic Climate Change in CMIP6 Strikingly Intensified by NEMO-Family Climate Models, Geophys. Res. Lett., 50, e2022GL102077, https://doi.org/10.1029/2022GL102077, 2023.

Peralta-Ferriz, C. and Woodgate, R. A.: Seasonal and interannual variability of pan-Arctic surface mixed layer properties from 1979 to 2012 from hydrographic data, and the dominance of stratification for multiyear mixed layer depth shoaling, Prog. Oceanogr., 134, 19–53, https://doi.org/10.1016/j.pocean.2014.12.005, 2015.

Petersen, M. R., Asay-Davis, X. S., Berres, A. S., Chen, Q., Feige, N., Hoffman, M. J., Jacobsen, D. W., Jones, P. W., Maltrud, M. E., Price, S. F., Ringler, T. D., Streletz, G. J., Turner, A. K., Van Roekel, L. P., Veneziani, M., Wolfe, J. D., Wolfram, P. J., and Woodring, J. L.: An Evaluation of the Ocean and Sea Ice Climate of E3SM Using MPAS and Interannual CORE-II Forcing, J. Adv. Model. Earth Syst., 11, 1438–1458, https://doi.org/10.1029/2018MS001373, 2019.

Pnyushkov, A. V., Polyakov, I. V., Alekseev, G. V., Ashik, I. M., Baumann, T. M., Carmack, E. C., Ivanov, V. V., and Rember, R.: A Steady Regime of Volume and Heat Transports in the Eastern Arctic Ocean in the Early 21st Century, Front. Mar. Sci., 8, 705608, https://doi.org/10.3389/fmars.2021.705608, 2021.

Polyakov, I. V., Beszczynska, A., Carmack, E. C., Dmitrenko, I. A., Fahrbach, E., Frolov, I. E., Gerdes, R., Hansen, E., Holfort, J., Ivanov, V. V., Johnson, M. A., Karcher, M., Kauker, F., Morison, J., Orvik, K. A., Schauer, U., Simmons, H. L., Skagseth, Ø., Sokolov, V. T., Steele, M., Timokhov, L. A., Walsh, D., and Walsh, J. E.: One more step toward a warmer Arctic, Geophys. Res. Lett., 32, 2005GL023740, https://doi.org/10.1029/2005GL023740, 2005.

Polyakov, I. V., Timokhov, L. A., Alexeev, V. A., Bacon, S., Dmitrenko, I. A., Fortier, L., Frolov, I. E., Gascard, J.-C., Hansen, E., Ivanov, V. V., Laxon, S., Mauritzen, C., Perovich, D., Shimada, K., Simmons, H. L., Sokolov, V. T., Steele, M., and Toole, J.: Arctic Ocean Warming Contributes to Reduced Polar Ice Cap, J. Phys. Oceanogr., 40, 2743–2756, https://doi.org/10.1175/2010JPO4339.1, 2010.

Polyakov, I. V., Bhatt, U. S., Walsh, J. E., Abrahamsen, E. P., Pnyushkov, A. V., and Wassmann, P. F.: Recent oceanic changes

in the Arctic in the context of long-term observations, Ecol. Appl., 23, 1745–1764, https://doi.org/10.1890/11-0902.1, 2013.

Polyakov, I. V., Pnyushkov, A. V., Alkire, M. B., Ashik, I. M., Baumann, T. M., Carmack, E. C., Goszczko, I., Guthrie, J., Ivanov, V. V., Kanzow, T., Krishfield, R., Kwok, R., Sundfjord, A., Morison, J., Rember, R., and Yulin, A.: Greater role for Atlantic inflows on sea-ice loss in the Eurasian Basin of the Arctic Ocean, Science, 356, 285–291, https://doi.org/10.1126/science.aai8204, 2017.

Polyakov, I. V., Alkire, M. B., Bluhm, B. A., Brown, K. A., Carmack, E. C., Chierici, M., Danielson, S. L., Ellingsen, I., Ershova, E. A., Gårdfeldt, K., Ingvaldsen, R. B., Pnyushkov, A. V., Slagstad, D., and Wassmann, P.: Borealization of the Arctic Ocean in Response to Anomalous Advection From Sub-Arctic Seas, Front. Mar. Sci., 7, 491, https://doi.org/10.3389/fmars.2020.00491, 2020a.

Polyakov, I. V., Rippeth, T. P., Fer, I., Alkire, M. B., Baumann, T. M., Carmack, E. C., Ingvaldsen, R., Ivanov, V. V., Janout, M., Lind, S., Padman, L., Pnyushkov, A. V., and Rember, R.: Weakening of Cold Halocline Layer Exposes Sea Ice to Oceanic Heat in the Eastern Arctic Ocean, J. Climate, 33, 8107–8123, https://doi.org/10.1175/JCLI-D-19-0976.1, 2020b.

Polyakov, I. V., Mayer, M., Tietsche, S., and Karpechko, A. Yu.: Climate Change Fosters Competing Effects of Dynamics and Thermodynamics in Seasonal Predictability of Arctic Sea Ice, J. Climate, 35, 2849–2865, https://doi.org/10.1175/JCLI-D-21-0463.1, 2022.

Polyakov, I. V., Pnyushkov, A. V., Charette, M., Cho, K.-H., Jung, J., Kipp, L., Muilwijk, M., Whitmore, L., Yang, E. J., and Yoo, J.: Atlantification advances into the Amerasian Basin of the Arctic Ocean, Sci. Adv., 11, eadq7580, https://doi.org/10.1126/sciadv.adq7580, 2025.

Proshutinsky, A., Krishfield, R., Toole, J. M., Timmermans, M. -L., Williams, W., Zimmermann, S., Yamamoto-Kawai, M., Armitage, T. W. K., Dukhovskoy, D., Golubeva, E., Manucharyan, G. E., Platov, G., Watanabe, E., Kikuchi, T., Nishino, S., Itoh, M., Kang, S. -H., Cho, K. -H., Tateyama, K., and Zhao, J.: Analysis of the Beaufort Gyre Freshwater Content in 2003–2018, J. Geophys. Res.-Oceans, 124, 9658–9689, https://doi.org/10.1029/2019JC015281, 2019.

Rantanen, M., Karpechko, A. Yu., Lipponen, A., Nordling, K., Hyvärinen, O., Ruosteenoja, K., Vihma, T., and Laaksonen, A.: The Arctic has warmed nearly four times faster than the globe since 1979, Commun. Earth Environ., 3, 168, https://doi.org/10.1038/s43247-022-00498-3, 2022.

Rayner, N. A., Parker, D. E., Horton, E. B., Folland, C. K., Alexander, L. V., Rowell, D. P., Kent, E. C., and Kaplan, A.: Global analyses of sea surface temperature, sea ice, and night marine air temperature since the late nineteenth century, J. Geophys. Res., 108, 2002JD002670, https://doi.org/10.1029/2002JD002670, 2003.

Reagan, J. R., Seidov, D., Wang, Z., Dukhovskoy, D., Boyer, T. P., Locarnini, R. A., Baranova, O. K., Mishonov, A. V., Garcia, H. E., Bouchard, C., Cross, S. L., and Paver, C. R.: World Ocean Atlas 2023, Volume 2: Salinity, NOAA, https://doi.org/10.25923/70QT-9574, 2024.

Richards, A. E., Johnson, H. L., and Lique, C.: Spatial and Temporal Variability of Atlantic Water in the Arctic From 40 Years of Observations, J. Geophys. Res.-Oceans, 127, e2021JC018358, https://doi.org/10.1029/2021JC018358, 2022.

Ricker, R., Hendricks, S., Kaleschke, L., Tian-Kunze, X., King, J., and Haas, C.: A weekly Arctic sea-ice thickness data record from merged CryoSat-2 and SMOS satellite data, The Cryosphere, 11, 1607–1623, https://doi.org/10.5194/tc-11-1607-2017, 2017.

Rieke, O., Årthun, M., and Dörr, J. S.: Rapid sea ice changes in the future Barents Sea, The Cryosphere, 17, 1445–1456, https://doi.org/10.5194/tc-17-1445-2023, 2023.

Ringler, T., Petersen, M., Higdon, R. L., Jacobsen, D., Jones, P. W., and Maltrud, M.: A multi-resolution approach to global ocean modeling, Ocean Model., 69, 211–232, https://doi.org/10.1016/j.ocemod.2013.04.010, 2013.

Schauer, U., Fahrbach, E., Osterhus, S., and Rohardt, G.: Arctic warming through the Fram Strait: Oceanic heat transport from 3 years of measurements, J. Geophys. Res., 109, 2003JC001823, https://doi.org/10.1029/2003JC001823, 2004.

Schauer, U., Beszczynska-Möller, A., Walczowski, W., Fahrbach, E., Piechura, J., and Hansen, E.: Variation of Measured Heat Flow Through the Fram Strait Between 1997 and 2006, in: Arctic–Subarctic Ocean Fluxes: Defining the Role of the Northern Seas in Climate, edited by: Dickson, R. R., Meincke, J., and Rhines, P., Springer Netherlands, Dordrecht, 65–85, https://doi.org/10.1007/978-1-4020-6774-7_4, 2008.

Scholz, P., Sidorenko, D., Gurses, O., Danilov, S., Koldunov, N., Wang, Q., Sein, D., Smolentseva, M., Rakowsky, N., and Jung, T.: Assessment of the Finite-volumE Sea ice-Ocean Model (FESOM2.0) – Part 1: Description of selected key model elements and comparison to its predecessor version, Geosci. Model Dev., 12, 4875–4899, https://doi.org/10.5194/gmd-12-4875-2019, 2019.

Schweiger, A., Lindsay, R., Zhang, J., Steele, M., Stern, H., and Kwok, R.: Uncertainty in modeled Arctic sea ice volume, J. Geophys. Res., 116, C00D06, https://doi.org/10.1029/2011JC007084, 2011.

Schweiger, A. J., Wood, K. R., and Zhang, J.: Arctic Sea Ice Volume Variability over 1901–2010: A Model-Based Reconstruction, J. Climate, 32, 4731–4752, https://doi.org/10.1175/JCLI-D-19-0008.1, 2019.

Shu, Q., Wang, Q., Su, J., Li, X., and Qiao, F.: Assessment of the Atlantic water layer in the Arctic Ocean in CMIP5 climate models, Clim. Dynam., 53, 5279–5291, https://doi.org/10.1007/s00382-019-04870-6, 2019.

Shu, Q., Wang, Q., Årthun, M., Wang, S., Song, Z., Zhang, M., and Qiao, F.: Arctic Ocean Amplification in a warming climate in CMIP6 models, Sci. Adv., 8, eabn9755, https://doi.org/10.1126/sciadv.abn9755, 2022.

Smedsrud, L. H., Esau, I., Ingvaldsen, R. B., Eldevik, T., Haugan, P. M., Li, C., Lien, V. S., Olsen, A., Omar, A. M., Otterå, O. H., Risebrobakken, B., Sandø, A. B., Semenov, V. A., and Sorokina, S. A.: The role of the Barents Sea in the arctic climate system, Rev. Geophys., 51, 415–449, https://doi.org/10.1002/rog.20017, 2013.

Steele, M. and Boyd, T.: Retreat of the cold halocline layer in the Arctic Ocean, J. Geophys. Res., 103, 10419–10435, https://doi.org/10.1029/98JC00580, 1998.

Steele, M., Morley, R., and Ermold, W.: PHC: A Global Ocean Hydrography with a High-Quality Arctic Ocean, J. Climate, 14, 2079–2087, https://doi.org/10.1175/1520-0442(2001)014<2079:PAGOHW>2.0.CO;2, 2001.

Stroeve, J., Barrett, A., Serreze, M., and Schweiger, A.: Using records from submarine, aircraft and satellites to evaluate climate model simulations of Arctic sea ice thickness, The Cryosphere, 8, 1839–1854, https://doi.org/10.5194/tc-8-1839-2014, 2014.

Tsubouchi, T., Von Appen, W.-J., Kanzow, T., and De Steur, L.: Temporal Variability of the Overturning Circulation in the Arctic Ocean and the Associated Heat and Freshwater Transports during 2004–10, J. Phys. Oceanogr., 54, 81–94, https://doi.org/10.1175/JPO-D-23-0056.1, 2024.

Tsujino, H., Urakawa, S., Nakano, H., Small, R. J., Kim, W. M., Yeager, S. G., Danabasoglu, G., Suzuki, T., Bamber, J. L., Bentsen, M., Böning, C. W., Bozec, A., Chassignet, E. P., Curchitser, E., Boeira Dias, F., Durack, P. J., Griffies, S. M., Harada, Y., Ilicak, M., Josey, S. A., Kobayashi, C., Kobayashi, S., Komuro, Y., Large, W. G., Le Sommer, J., Marsland, S. J., Masina, S., Scheinert, M., Tomita, H., Valdivieso, M., and Yamazaki, D.: JRA-55 based surface dataset for driving ocean–sea-ice models (JRA55-do), Ocean Model., 130, 79–139, https://doi.org/10.1016/j.ocemod.2018.07.002, 2018.

Turner, A. K., Lipscomb, W. H., Hunke, E. C., Jacobsen, D. W., Jeffery, N., Engwirda, D., Ringler, T. D., and Wolfe, J. D.: MPAS-Seaice (v1.0.0): sea-ice dynamics on unstructured Voronoi meshes, Geosci. Model Dev., 15, 3721–3751, https://doi.org/10.5194/gmd-15-3721-2022, 2022.

Turner, J. S.: The Melting of Ice in the Arctic Ocean: The Influence of Double-Diffusive Transport of Heat from Below, J. Phys. Oceanogr., 40, 249–256, https://doi.org/10.1175/2009JPO4279.1, 2010.

Veneziani, M., Maslowski, W., Lee, Y. J., D'Angelo, G., Osinski, R., Petersen, M. R., Weijer, W., Craig, A. P., Wolfe, J. D., Comeau, D., and Turner, A. K.: An evaluation of the E3SMv1 Arctic ocean and sea-ice regionally refined model, Geosci. Model Dev., 15, 3133–3160, https://doi.org/10.5194/gmd-15-3133-2022, 2022.

Von Schuckmann, K., Cheng, L., Palmer, M. D., Hansen, J., Tassone, C., Aich, V., Adusumilli, S., Beltrami, H., Boyer, T., Cuesta-Valero, F. J., Desbruyères, D., Domingues, C., García-García, A., Gentine, P., Gilson, J., Gorfer, M., Haimberger, L., Ishii, M., Johnson, G. C., Killick, R., King, B. A., Kirchengast, G., Kolodziejczyk, N., Lyman, J., Marzeion, B., Mayer, M., Monier, M., Monselesan, D. P., Purkey, S., Roemmich, D., Schweiger, A., Seneviratne, S. I., Shepherd, A., Slater, D. A., Steiner, A. K., Straneo, F., Timmermans, M.-L., and Wijffels, S. E.: Heat stored in the Earth system: where does the energy go?, Earth Syst. Sci. Data, 12, 2013–2041, https://doi.org/10.5194/essd-12-2013-2020, 2020.

Wang, Q., Wekerle, C., Danilov, S., Wang, X., and Jung, T.: A 4.5 km resolution Arctic Ocean simulation with the global multi-resolution model FESOM 1.4, Geosci. Model Dev., 11, 1229–1255, https://doi.org/10.5194/gmd-11-1229-2018, 2018.

Wang, Q., Wekerle, C., Danilov, S., Sidorenko, D., Koldunov, N., Sein, D., Rabe, B., and Jung, T.: Recent Sea Ice Decline Did Not Significantly Increase the Total Liquid Freshwater Content of the Arctic Ocean, J. Climate, 32, 15–32, https://doi.org/10.1175/JCLI-D-18-0237.1, 2019.

Wang, Q., Shu, Q., Danilov, S., and Sidorenko, D.: An extreme event of enhanced Arctic Ocean export west of Greenland caused by the pronounced dynamic sea level drop in the North Atlantic subpolar gyre in the mid-to-late 2010s, Environ. Res. Lett., 17, 044046, https://doi.org/10.1088/1748-9326/ac5562, 2022.

Wang, Q., Shu, Q., Wang, S., Beszczynska-Moeller, A., Danilov, S., Steur, L., Haine, T. W. N., Karcher, M., Lee, C. M., Myers, P. G., Polyakov, I. V., Provost, C., Skagseth, Ø., Spreen, G., and Woodgate, R.: A Review of Arctic–Subarctic Ocean Linkages: Past Changes, Mechanisms, and Future Projections, Ocean-Land-Atmos. Res., 2, 0013, https://doi.org/10.34133/olar.0013, 2023.

Wang, Q., Shu, Q., Bozec, A., Chassignet, E. P., Fogli, P. G., Fox-Kemper, B., McHogg, A. C., Iovino, D., Kiss, A. E., Koldunov, N., Le Sommer, J., Li, Y., Lin, P., Liu, H., Polyakov, I., Scholz, P., Sidorenko, D., Wang, S., and Xu, X.: Impact of increased resolution on Arctic Ocean simulations in Ocean Model Intercomparison Project phase 2 (OMIP-2), Geosci. Model Dev., 17, 347–379, https://doi.org/10.5194/gmd-17-347-2024, 2024.

Wassmann, P., Kosobokova, K. N., Slagstad, D., Drinkwater, K. F., Hopcroft, R. R., Moore, S. E., Ellingsen, I., Nelson, R. J., Carmack, E., Popova, E., and Berge, J.: The contiguous domains of Arctic Ocean advection: Trails of life and death, Prog. Oceanogr., 139, 42–65, https://doi.org/10.1016/j.pocean.2015.06.011, 2015.

Wekerle, C., Wang, Q., Danilov, S., Jung, T., and Schröter, J.: The Canadian Arctic Archipelago throughflow in a multiresolution global model: Model assessment and the driving mechanism of interannual variability, J. Geophys. Res.-Oceans, 118, 4525–4541, https://doi.org/10.1002/jgrc.20330, 2013.

Woodgate, R. A.: Increases in the Pacific inflow to the Arctic from 1990 to 2015, and insights into seasonal trends and driving mechanisms from year-round Bering Strait mooring data, Prog. Oceanogr., 160, 124–154, https://doi.org/10.1016/j.pocean.2017.12.007, 2018.

Woodgate, R. A. and Peralta-Ferriz, C.: Warming and Freshening of the Pacific Inflow to the Arctic From 1990–2019 Implying Dramatic Shoaling in Pacific Winter Water Ventilation of the Arctic Water Column, Geophys. Res. Lett., 48, e2021GL092528, https://doi.org/10.1029/2021GL092528, 2021.

Zhang, J. and Rothrock, D. A.: Modeling Global Sea Ice with a Thickness and Enthalpy Distribution Model in Generalized Curvilinear Coordinates, Mon. Weather Rev., 131, 845–861, https://doi.org/10.1175/1520-0493(2003)131<0845:MGSIWA>2.0.CO;2, 2003.

Zhang, Y., Chen, C., Beardsley, R. C., Gao, G., Qi, J., and Lin, H.: Seasonal and interannual variability of the Arctic sea ice: A comparison between AO-FVCOM and observations: Numerical study on the Arctic sea ice, J. Geophys. Res.-Oceans, 121, 8320–8350, https://doi.org/10.1002/2016JC011841, 2016.

Zhu, Y., Zhang, R.-H., Moum, J. N., Wang, F., Li, X., and Li, D.: Physics-informed deep-learning parameterization of ocean vertical mixing improves climate simulations, Natl. Sci. Rev., 9, nwac044, https://doi.org/10.1093/nsr/nwac044, 2022.

Zuo, H., Balmaseda, M. A., Tietsche, S., Mogensen, K., and Mayer, M.: The ECMWF operational ensemble reanalysis–analysis system for ocean and sea ice: a description of the system and assessment, Ocean Sci., 15, 779–808, https://doi.org/10.5194/os-15-779-2019, 2019.